Computers and Geotechnics 143 (2022) 104631

Contents lists available at ScienceDirect

Computers and Geotechnics

journal homepage: www.elsevier.com/locate/compgeo

# Rayleigh Wave-Shear Wave Coupling Mechanism for Large Lateral Deformation in Level Liquefiable Ground

Yunyi Li [a], Chao Luo [b,c], Jian-Min Zhang [a], Fang Liu [d], Rui Wang [a,*]

[a] Department of Hydraulic Engineering, State Key Laboratory of Hydroscience and Engineering, Tsinghua University, Beijing 100084, China
[b] State Key Laboratory of Mechanical Behavior and System Safety of Traffic Engineering Structures, Shijiazhuang Tiedao University, Shijiazhuang, Hebei Province 050043, China
[c] School of Civil Engineering, Shijiazhuang Tiedao University, Shijiazhuang, Hebei Province 050043, China
[d] State Key Laboratory of Disaster Reduction in Civil Engineering, Tongji University, Shanghai 200092, China

ARTICLE INFO

*Keywords:*
Liquefiable soil
Rayleigh wave
Shear wave
Level ground
Lateral deformation

ABSTRACT

Large lateral deformation in almost level liquefiable ground has been observed during past strong earthquakes, which cannot be explained by the same driving force as that in sloping ground. This study proposes a Rayleigh wave-shear wave coupling mechanism for this phenomenon, which is evaluated on the element and site levels. A simple element level elasto-plastic force–displacement model reveals that the combination of the symmetrical shear force with the asymmetrical shear resistance under Rayleigh wave-shear wave coupling can be a major contributor for the accumulation of lateral soil deformation. Finite element method numerical results for a site level ground model shows that Rayleigh wave-shear wave coupling can induce significantly greater lateral displacement compared to pure shear wave input, and further highlight the importance of soil liquefaction for this phenomenon. The amplitudes and frequencies of the shear wave and the Rayleigh wave and their phase difference are shown to affect the accumulation of lateral deformation. The findings of Rayleigh wave-shear wave coupling induced lateral deformation are consistent with observations in past earthquakes, and should be considered in geotechnical earthquake engineering.

## 1. Introduction

Large lateral deformation has been widely observed in liquefiable ground during strong earthquakes (e.g., Wang et al., 1983; Yoshida et al., 1992; Eberhard et al., 2010). This deformation is often considered to be caused by the initial static shear stress within soils in sloping ground or backfills behind retaining walls (Chiaro et al., 2013; Iai, 2018). However, large lateral deformation has also been observed in almost level ground in several earthquakes (Hamada, 1992; Zhang and Tokimatsu, 1998; Pei et al., 2017; Sassa and Takagawa, 2019), where the initial static shear stress is negligible.

For example, in the 2018 Sulawesi Earthquake, several cases of large-scale liquefaction-induced lateral deformations were observed (e.g., Sassa and Takagawa, 2019; Bradley et al., 2019; Socquet et al., 2019; Wang et al., 2019; Yolsal-Cevikbilen and Taymaz, 2019; Gallant et al., 2020; Lombardo and Tanyas, 2020). Kilometer-scale lateral deformation occurred in very mildly sloping areas with inclination angle largely below 2°. Sassa and Takagawa (2019) suggested that the slides were largely due to liquefied gravity flow, yet deformation of this magnitude is rarely observed in laboratory experiments of medium dense liquefiable sandy ground of 2° to 5° slope, such as in the VELACS and LEAP experiments (e.g., Arulanandan, 1993; Kutter et al., 2020; He et al., 2020). Bradley et al. (2019), Watkinson and Hall (2019), and Gallant et al. (2020) suggested that communal and rice field irrigation were the cause for the huge flow slide. However, there were slide sites in Balaroa that were not associated with irrigation (Kiyota et al., 2020). Surface wave, e.g., Rayleigh wave, was observed during the Sulawesi earthquake (Han et al., 2019; Kusumawardani et al., 2021), the effect of which has not yet been considered for the generation of large lateral ground deformation. Unlike the symmetric lateral motion of shear waves, Rayleigh waves can generate horizontally asymmetrical dynamic motion within the ground (Brune and Pomeroy, 1963), which may also be a triggering factor for the observed large lateral ground deformation in nearly flat ground.

* Corresponding author.
*E-mail addresses:* liyunyi16@mails.tsinghua.edu.cn (Y. Li), luochao@stdu.edu.cn (C. Luo), zhangjm@mail.tsinghua.edu.cn (J.-M. Zhang), liufang@tongji.edu.cn (F. Liu), wangrui_05@mail.tsinghua.edu.cn (R. Wang).

https://doi.org/10.1016/j.compgeo.2022.104631
Received 2 July 2021; Received in revised form 30 December 2021; Accepted 31 December 2021
Available online 11 January 2022

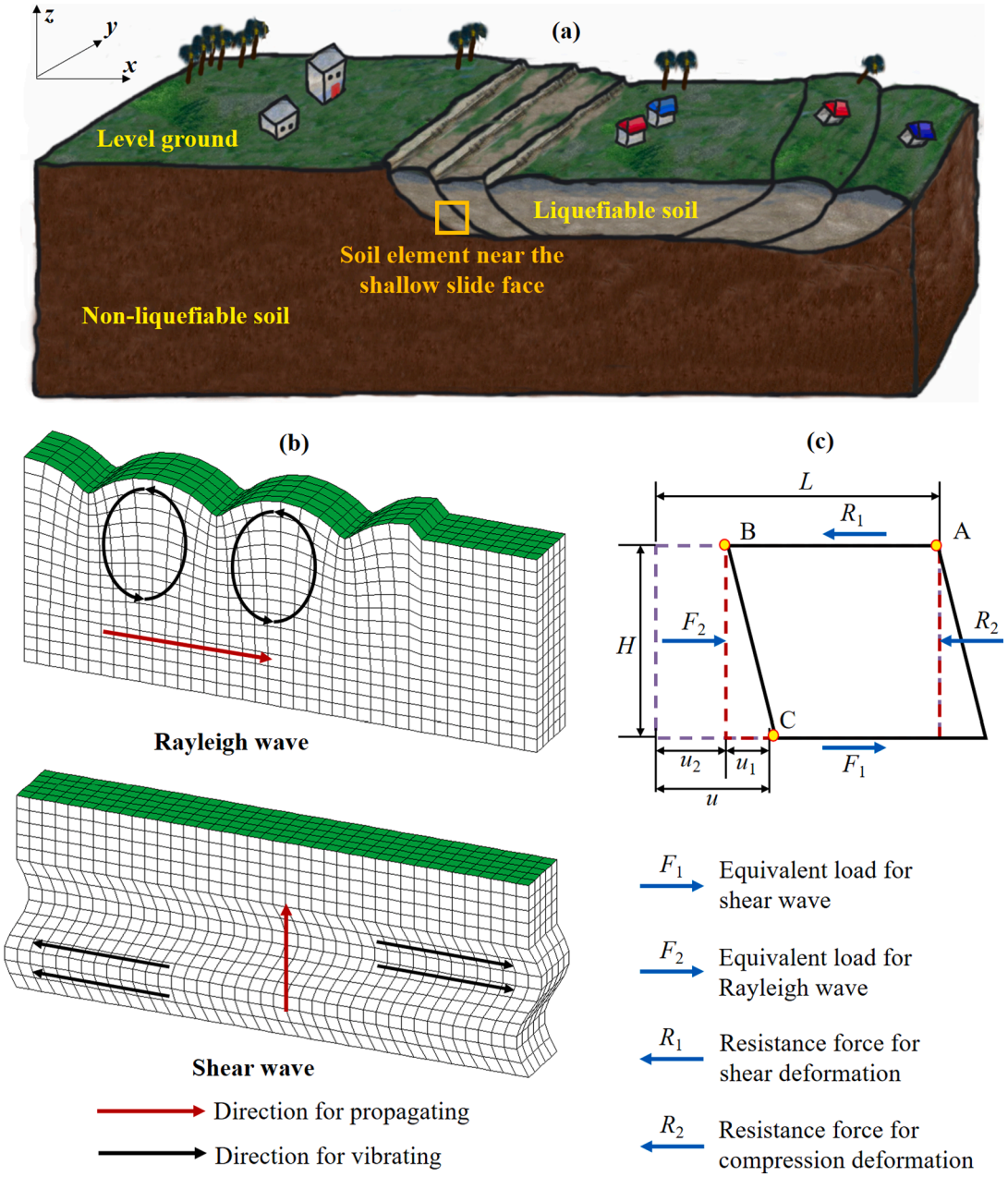


**Fig. 1.** Schematic diagrams for soil motion and force–displacement under Rayleigh wave and shear wave (a) a typical seismic-wave-caused shallow sliding in a level liquefiable ground; (b) soil motion under Rayleigh wave and shear wave; (c) force–displacement of a soil element under Rayleigh wave and shear wave.

In this study, we hypothesize that the characteristics of the seismic wave at the site can be a crucial factor contributing to the lateral deformation of level or very mildly sloping liquefiable ground. Although existing studies have highlighted the significance of surface waves in causing soil to liquefy, the influence of surface waves on the deformation of liquefiable ground has yet to be evaluated. Fang et al. (1979) and Wang et al. (1983) identified soil liquefaction caused by surface waves from aerial photographs of the 1976 Tangshan Earthquake. Men (1992) confirmed that some sand boils on ground surface in the 1976 Tangshan Earthquake were caused by Rayleigh waves. Wolf (1985) suggested that Rayleigh wave could cause greater peak shear stress than shear wave at shallow depths. Staroszczyk (1996, 2016) assessed the development of excess pore pressures and liquefaction in level sandy ground under Rayleigh waves. Cui et al. (2004) pointed out that Rayleigh waves can be an important cause of liquefaction in shallow saturated sandy deposit. Jiang et al. (2021) compared the liquefaction potential of granular material under SH wave and Love wave type loading using the discrete element method, and suggested that effective stress reduction can occur more rapidly under multi-direction loading caused by surface waves. To assess liquefiable ground deformation under surface waves, high-fidelity constitutive models for the liquefaction behavior of sand must be adopted. This is achieved in the current study by adopting the CycLiq model of Wang et al. (2014), which has been shown to be effective for simulating large post-liquefaction deformations (e.g., Wang et al., 2016; Zhu et al., 2021; Liu et al., 2020).

This study aims to analyze the effect of shear waves, Rayleigh waves, and their coupling on the lateral deformation in level liquefiable ground to provide a new perspective for explaining the large lateral deformation observed in almost level grounds during earthquakes. A simple element level force–displacement model using linear elastic, elastic-perfectly-plastic, and CycLiq constitutive models, respectively, is first used to explain the physics of asymmetrical deformation accumulation under

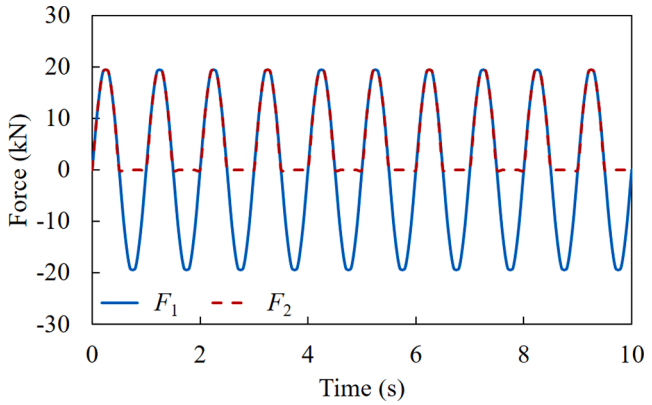


**Fig. 2.** Time histories of $F_1$ and $F_2$ for the force–displacement element model.

Rayleigh wave-shear wave coupling in Section 2. A finite element model, using the CycLiq constitutive model for liquefaction behavior of sand and viscous-spring artificial boundary conditions for non-uniform seismic wave input, is then proposed in Section 3 to analyze the behavior of liquefiable ground under various forms of seismic input for a typical level liquefiable ground. The computed displacements, strains, and stresses under different forms of seismic waves are analyzed in detail in Section 4, revealing the influence of Rayleigh wave and its coupling with shear wave on the lateral deformation in level liquefiable ground. Section 5 discusses the influence of shear wave and the Rayleigh wave amplitudes, frequencies and their phase difference on lateral deformation.

## 2. Element level explanation for the influence of Rayleigh wave-shear wave coupling on soil deformation

The hypothesis that Rayleigh wave input can contribute to the generation of large lateral deformation in liquefiable soil is first assessed in this section on an element level, as a proof of concept. For a typical seismic-wave-caused shallow slide in level liquefiable ground shown in Fig. 1(a), shear waves induce horizontal shear force in the soil, whereas Rayleigh waves induce horizontal compressive normal force, as shown in Fig. 1(b).

As illustrated in Fig. 1(c), an element level force–displacement model is constructed in to consider the influence of shear wave and Rayleigh wave induced loads on soil deformation near the shallow slide face. At shallow depths near the ground surface, a shear wave generates horizontal shear load $F_1$ on the element, while a Rayleigh wave generates a horizontal compression load $F_2$. $R_1$ and $R_2$ are the resistance forces generated by the soil as the element deforms in shear and compression, respectively. The vertical forces induced by Rayleigh wave acting on the element are less than 5% of the gravitational stress, numerical investigations show that the influence of vertical forces is insignificant. Thus, the vertical forces are considered constant here for simplicity. Assuming point A to be fixed, the total displacement $u$ caused by shear and compression is the relative displacement between A and C. Displacement components $u_1$ and $u_2$ represent relative displacement caused by shear and compression deformation, respectively, with $u = u_1 + u_2$. $L$ and $H$ are the length and height of the element, respectively.

The dynamic equilibrium equations for the force–displacement model are:

$$\rho HL\ddot{u}_1 = F_1 - R_1 - c\dot{u}_1 \tag{1a}$$

$$\rho HL\ddot{u}_2 = F_2 - R_2 - c\dot{u}_2 \tag{1b}$$

where $\rho$ is the soil density and $c$ is the damping coefficient. These two differential equations can be solved with a central difference time-integration method, once the loads $F_1$ and $F_2$ and resistance forces $R_1$ and $R_2$ are determined as described in Section 2.1 and 2.2.

### 2.1. Seismic wave induced loads

Without losing generality, the shear and compression loads generated by shear wave and Rayleigh wave, respectively, are considered sinusoidal. Sand does not usually possess tensile strength, so both $F_2$ and $R_2$ must remain non-negative. Here, positive value refers to compression in accordance to the sign conventions of soil mechanics. Thus, the loads are expressed as:

$$F_1 = A_1 sin(\omega_1 t + \theta) \tag{2a}$$

$$F_2 = max[A_2 sin(\omega_2 t), 0] \tag{2b}$$

where $A_1$ and $A_2$ are the amplitudes of input loads, $\omega_1$ and $\omega_2$ are the circular frequencies of loads, which are considered to be the same for the element level analysis for simplicity, i.e., $\omega_1 = \omega_2 = \omega$, and $\theta$ is the phase difference between shear wave and Rayleigh wave. For a 2-D problem in the $x$-$z$ plane, shear wave travels vertically (i.e., along the $z$ direction) and Rayleigh wave travels horizontally (i.e., along the $x$ direction). The general solutions of displacements $u_S$ under single direction traveling shear wave and $u_R$ under Rayleigh wave at any point $(x_0, z_0)$ and time $t$ are expressed as:

$$u_S(x_0, z_0, t) = f(\omega_1 t - \xi_S z_0) \tag{3a}$$

$$u_R(x_0, z_0, t) = h(z_0) g(\omega_2 t - \xi_R x_0) \tag{3b}$$

where $f(*)$ and $g(*)$ are the general solutions of wave equations under shear wave and Rayleigh wave, respectively. $h(*)$ is the distribution function of Rayleigh wave along depth, which is constant with time. $\xi_S$ and $\xi_R$ are the wave numbers of shear wave and Rayleigh wave, respectively. In Eq. (3-a) and (3-b), if $\omega_1 = \omega_2 = \omega$ and the phase of Rayleigh wave is set as 0° at $t = 0$ s and $x_0 = 0$, the phase difference $\theta$ is determined by $x_0$ and $z_0$:

$$\theta = \xi_R x_0 - \xi_S z_0 \tag{4}$$

Therefore, $\theta$ would vary depending on the relative locations of the source of earthquake and the location of the site. It is assumed in this section that $\theta = 0°$ for the element level analysis for simplicity.

In the element level analysis of this section, for loads $F_1$ and $F_2$, assume $A_1 = A_2 = 20$ kN, $\omega = 2\pi$ rad/s, $\theta = 0°$, with time histories shown in Fig. 2. As Eq. (2) dictates, $F_1$ is symmetrical and $F_2$ is asymmetrical due to sand being unable to withstand tension. $F_1$ and $F_2$ can be input independently or in combination to simulate the input from a shear wave, a Rayleigh wave, or a combination of both.

### 2.2. Calculation of resistance forces

The resistance forces $R_1$ and $R_2$ are dictated by the constitutive behavior of the soil element. In this section, three different types of constitutive models are used on the element level to assess the influence of shear wave and Rayleigh wave coupling. The linear elastic model is used as a benchmark, the elastic-perfectly plastic model using the von Mises yield criterion to provide a simple illustration for the role of plasticity in Rayleigh wave induced deformation, the high fidelity CycLiq model is finally adopted to provide a realistic assessment of Rayleigh wave induced deformation in liquefiable soil.

It is assumed that stresses and strains are homogeneous in the element, such that:

$$u_1 = \gamma H \tag{5a}$$

$$u_2 = \varepsilon L \tag{5b}$$

$$R_1 = \tau L \tag{5c}$$

**Table 1**
Parameters of the unified plasticity model for liquefaction behavior of sand.

| Parameter | Value | Category |
|---|---|---|
| $G_0$ | 200 kPa | Parameters for elastic modulus |
| $\kappa$ | 0.008 | |
| $h$ | 1.8 | Parameters for plastic modulus |
| $n^p$ | 1.1 | |
| $M$ | 1.35 | Parameters for critical state |
| $\lambda$ | 0.019 | |
| $\xi$ | 0.7 | |
| $e_0$ | 0.934 | |
| $d_{re,1}$ | 0.1 | Parameters for dilatancy |
| $d_{re,2}$ | 30 | |
| $d_{ir}$ | 0.75 | |
| $\alpha$ | 10 | |
| $n^d$ | 7.8 | |
| $\gamma_{d,r}$ | 0.05 | Reference shear strain |
| $e_{in}$ | 0.8 | Initial void ratio |

$$R_2 = \sigma H \tag{5d}$$

where $\gamma$, $\varepsilon$, $\tau$, and $\sigma$ are shear strain, compression strain, shear stress, and compression stress, respectively. Specifically in the case analyzed here, assume $H = L = 1$ m, $\rho = 2.0$ g/cm$^3$, $c = 80$ kN/(m/s), the process of calculating $R_1$ and $R_2$ under the three different constitutive models are presented as follows:

(1). For linear elastic constitutive relation, shear deformation and compression deformation are decoupled:

$$\dot{\sigma} = E_s \dot{\varepsilon}^e \tag{6a}$$

$$\dot{\tau} = G\dot{\gamma}^e \tag{6b}$$

where $E_s$ is the compression modulus and $G$ is the shear modulus. The modulus is chosen based on typical undrained medium-stiff soil, i.e., $G = 20$ MPa, $E_s = 400$ MPa.

(2). For elastic-perfectly plastic constitutive relation with von Mises yield criterion, the formulation and parameters for elasticity are the same as above, while the yield surface is expressed as:

$$J_2 = \sigma^2/3 + \tau^2 = k^2 \tag{7}$$

where $k$ is the yield stress, set as 10 kPa in this section. The Drucker postulate and associated flow rule are also satisfied for the element:

$$\dot{\sigma}_{ij}\dot{\varepsilon}^p_{ij} = 0 \tag{8}$$

where the superscript $p$ represents the plastic strain component, the superscript $e$ represents the elastic strain component.

Using the elasto-perfectly-plastic model with von Mises yield criterion provides an intuitive means to illustrate the influence of wave type when plasticity is incurred, and could be easily verified against analytical solutions. It should be noted that the von Mises yield criterion is not directly applicable to liquefiable soil and is only used here as a proof of concept.

(3). For a more realistic representation of soil liquefaction behavior, the CycLiq model with parameters listed in Table 1 is also adopted. The parameters are chosen within the typical range of existing studies. For conciseness, a brief categorization for the model parameters is provided in Table 1, while the detailed

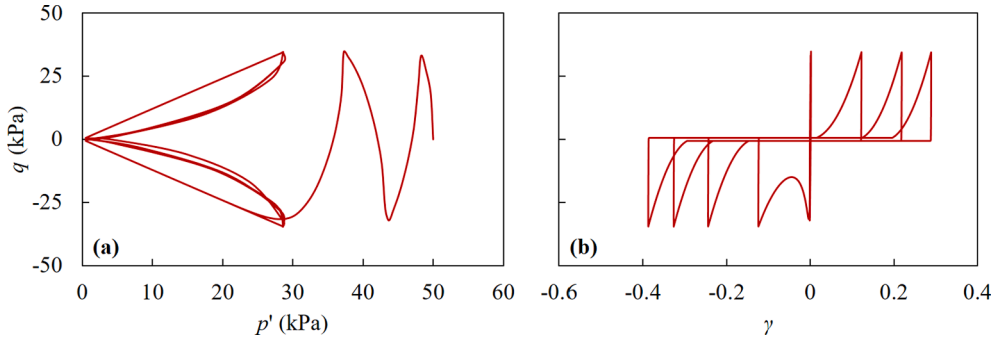


**Fig. 3.** Typical undrained cyclic torsional shear stress–strain response under initial confining stress of 50 kPa and deviatoric stress amplitude of 35 kPa, using the selected set of model parameters: (a) stress path in deviatoric stress $q$ and mean effective stress $p'$ space; (b) relationship between shear strain $\gamma$ and deviatoric stress $q$.

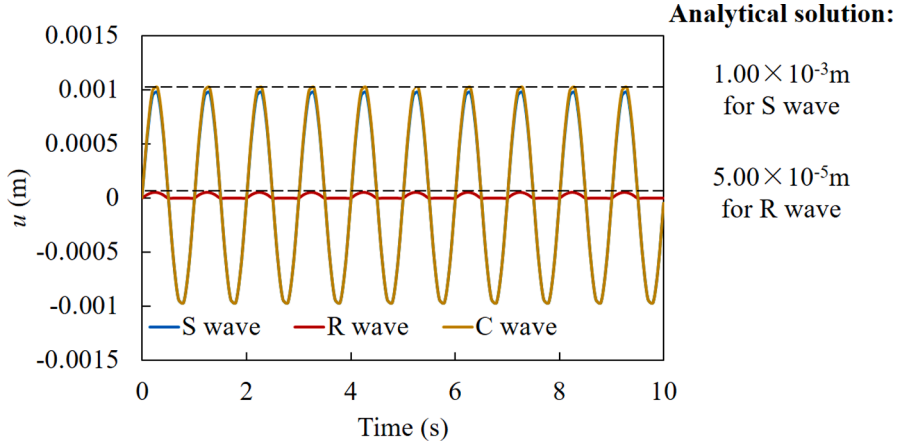


**Fig. 4.** Time histories of the total displacements $u$ for three different forms of input waves using force–displacement element model under linear elasticity.

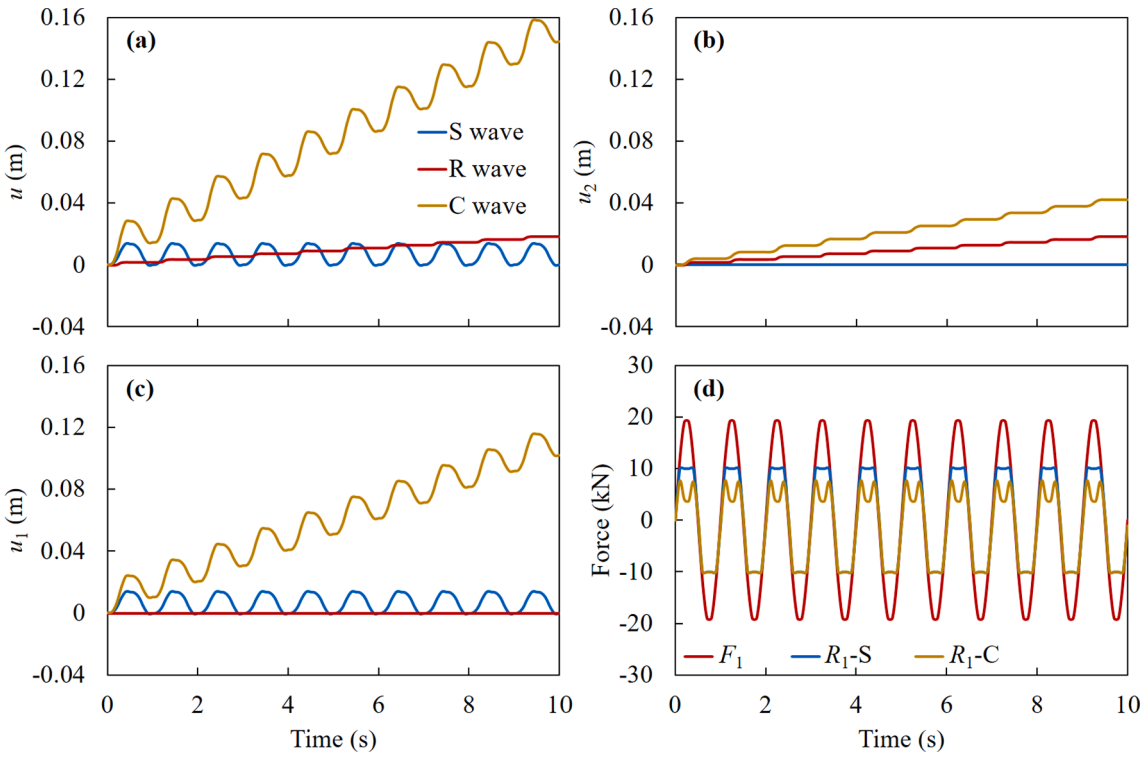


**Fig. 5.** Time histories of displacements and resistance forces for three different forms of input waves using force–displacement element model considering plasticity: (a) total displacement $u$; (b) compression induced displacement $u_2$; (c) shear induced displacement $u_1$; (d) $F_1$, and $R_1$ under pure shear wave ($R_1$-S) and combined wave ($R_1$-C).

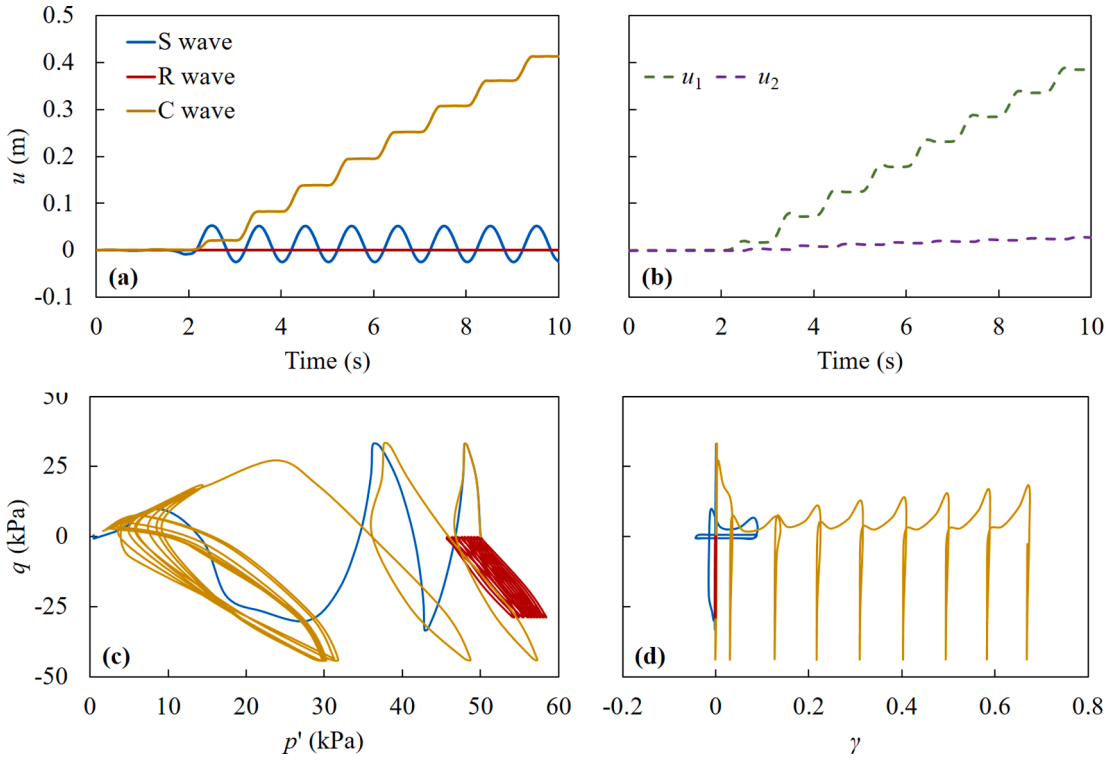


**Fig. 6.** Numerical simulation results of the force–displacement element model using the CycLiq model: (a) total displacement $u$ time histories under S wave, R wave, and C wave; (b) time histories of displacement components $u_1$ and $u_2$ under C wave; (c) stress path in deviatoric stress $q$ and mean effective stress $p'$ space under S wave, R wave, and C wave; (d) relationship between shear strain $\gamma$ and deviatoric stress $q$ under S wave, R wave, and C wave.

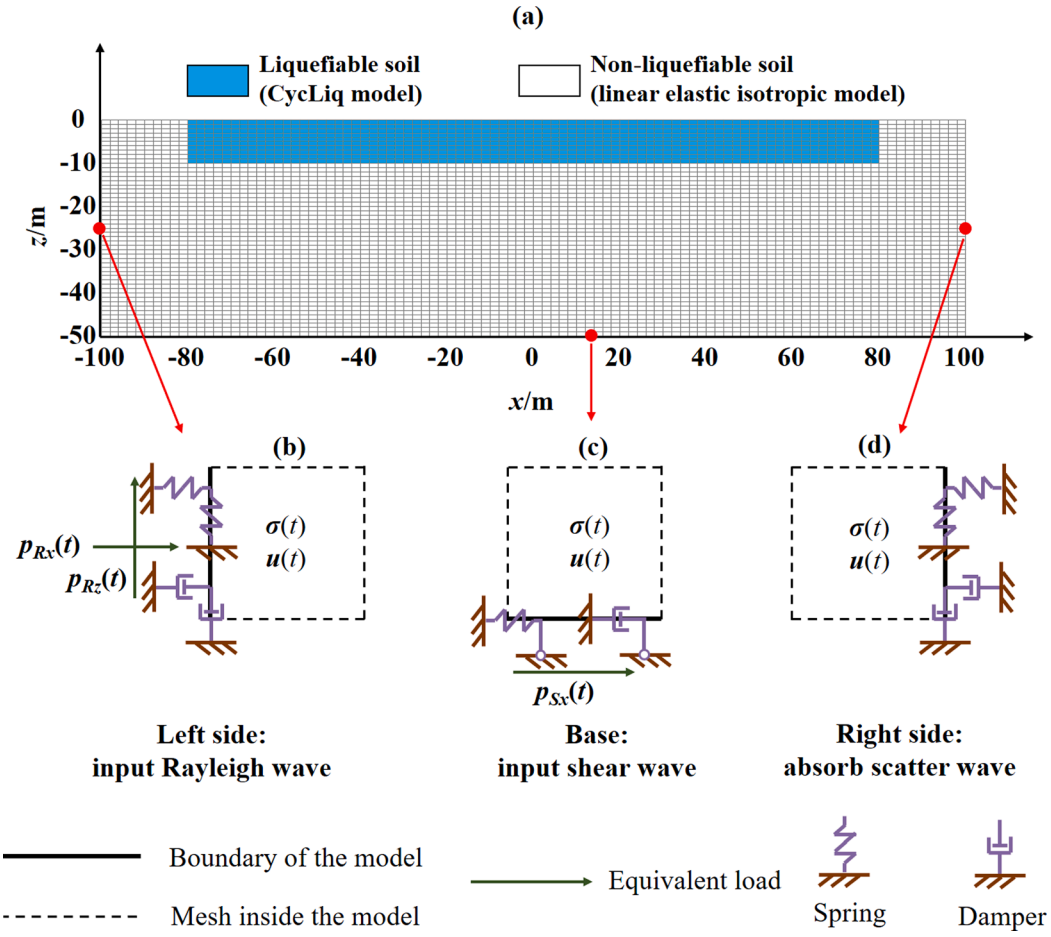


**Fig. 7.** Plane-strain solid–fluid coupled finite element analysis for a level liquefiable ground model under Rayleigh wave and shear wave: (a) the finite element mesh; (b) boundary condition at the left side; (c) boundary condition at the base; (d) boundary condition at the right side.

formulation of the model is not presented in this study, which can be found in detail in Wang et al. (2014, 2021).

To illustrate the cyclic behavior of sand captured by the CycLiq model for these given parameters, a numerical undrained cyclic torsional shear test under initial confining stress $p'$ of 50 kPa and deviatoric stress $q$ amplitude of 35 kPa is conducted. Here, $p' = (\sigma'_{11} + \sigma'_{22} + \sigma'_{33})/3$, $q = \text{sign}(\tau_{xz})\sqrt{3/2\mathbf{s} : \mathbf{s}}$, $\gamma = \text{sign}(\gamma_{xz})\sqrt{3/2\mathbf{e} : \mathbf{e}}$, where $\mathbf{s}$ and $\mathbf{e}$ is the deviatoric stress and strain tensor, the sign(*) function in the definition of $q$ and $\gamma$ is to reflect the direction of deviatoric stress and shear strain. Fig. 3 depicts the stress–strain curves in terms of both effective stress reduction and post-liquefaction shear deformation, which are shown to be representative of typical experimental results of sands (Zhang and Wang, 2012). The effective stress decreases during cyclic loading due to contraction, after initial liquefaction where mean effective stress $p'$ reaches zero for the first time, the "butterfly orbit" is observed (Fig. 3 (a)). At liquefaction state during each load cycle, the accumulation of large but bounded post-liquefaction shear strain $\gamma$ is observed in Fig. 3 (b). Note, the results in Fig. 3 are not quantitative simulations of any actual experiments.

### 2.3. Analysis results at the element level

As a benchmark case, the resulting time histories of the total displacement $u$ under pure shear wave (i.e., S wave), pure Rayleigh wave (i.e., R wave), and a combination of Rayleigh wave and shear wave (i.e., C wave) using linear elastic constitutive relation are shown in Fig. 4. The analytical solutions under S wave and R wave are provided in Appendix A. The displacement amplitudes of the analytical solutions are also marked in Fig. 4, which agrees with the numerical results to provide validation for the numerical solution. The displacement is oscillatory with no accumulation under all three forms of input waves, even though the input load for the Rayleigh wave and the combined wave are asymmetrical. The displacement under R wave is much smaller than that under S wave or C wave, because the compression modulus of saturated soft soil dynamic load is generally much greater than the shear modulus.

Fig. 5 shows the time-dependent displacements of a plastic element under elastic-perfectly plastic constitutive relation with von Mises yield criterion excited by different forms of waves. As shown in Fig. 5(a), no displacement accumulation is noted under S wave when plasticity is considered. In contrast, evident displacement accumulation occurs under R wave. The accumulated displacement is more significant for C wave, being an order of magnitude greater than that of R wave. The oscillatory displacement amplitude under C wave is close to that of S wave and much larger than that of R wave, agreeing with that of the elastic analysis.

Shear induced displacement $u_1$ and compression induced displacement $u_2$ for the three forms of input waves are compared in Fig. 5(b) and (c). The accumulation of $u_2$ under C wave is about twice that of R wave, while no accumulation is observed for S wave (Fig. 5(b)). However, the difference in cumulative compressive displacement alone does not explain the huge difference in the total displacement for C wave and R wave input. Unlike under the other two wave inputs, significant accumulation of $u_1$ occurs under the combination of R wave and S wave input (Fig. 5(c)). This indicates that the deformation accumulation under the combined wave is mainly generated via asymmetrical shear

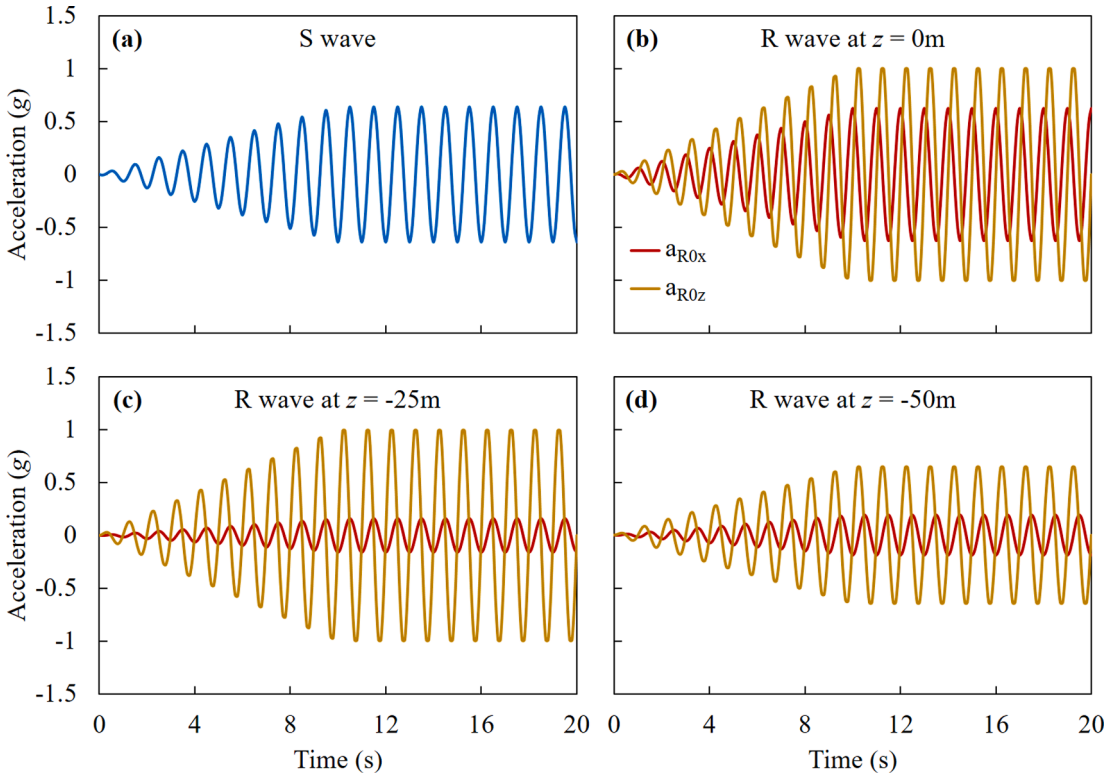


**Fig. 8.** Input shear wave and Rayleigh wave acceleration time histories: (a) input shear wave at the bottom boundary of the model; (b)-(d) input Rayleigh wave at the left boundary at different depths.

deformation, even though it is the input compression force that is asymmetrical.

Fig. 5(d) plots the shear resistance force $R_1$ under S wave and C wave in comparison with the input shear load $F_1$ to show the influence of compression-shear coupling under the combined wave. The shear wave induced load $F_1$ is the same and symmetrical for both forms of input, but $R_1$ becomes asymmetrical after adding the asymmetrical compression load $F_2$. For the plasticity model, although elastic compression and shear deformation are decoupled, the plastic deformation is affected by the coupling of the compression and shear stresses, and thus the asymmetric compression stress induced by the Rayleigh wave also causes the shear resistance $R_1$ to be asymmetrical ($R_1$-$C$ in Fig. 5(d)). Therefore, the combination of Rayleigh wave and shear wave greatly amplifies the effect of asymmetrical load from the Rayleigh wave on deformation accumulation.

The numerical results for the element analysis using the CycLiq constitutive model under undrained conditions with initial confining stress of 50 kPa are plotted in Fig. 6. Fig. 6 (a) and (b) presents similar displacement time history patterns using the CycLiq model as those in Fig. 5. Displacement oscillation is observed under S wave in Fig. 6 (a) without displacement accumulation, while the displacement under R wave is almost negligible. In contrast, significant displacement accumulation is evident under C wave, reaching over 0.4 m at $t = 10$ s. Fig. 6 (b) compares the shear induced displacement component $u_1$ and compression induced displacement component $u_2$ under C wave, and confirms once more that the large displacement accumulation is mainly induced by shear deformation $u_1$, and is much greater than $u_2$.

Fig. 6 (c) plots the effective stress paths in $q$-$p'$ space under S wave, R wave, and C wave. The effective stress $p'$ under both S wave and C wave approaches liquefaction during loading, while the decrease in effective stress is very limited under R wave. The high effective stress attained under R wave corresponds to relatively high modulus, thus resulting in the almost negligible deformation observed in Fig. 6 (a), which is also observed in the $q$-$\gamma$ stress–strain plot in Fig. 6 (d). Fig. 6 (d) highlights that although low effective stress is achieved under both S wave and C wave, and significant shear strain is observed at or near liquefaction state under both types of waves, the shear strain does not accumulate under S wave, while shear strain accumulation progresses with increasing load cycles under C wave. The results using the CycLiq model agrees qualitatively with the conceptual findings using the simple elastic-perfectly plastic constitutive relation, and clearly suggest that soil degradation and asymmetrical force and resistance under C wave can lead to shear strain accumulation of an order of magnitude greater than that under S wave on the element level. For an actual liquefiable level ground, this type of deformation accumulation at the element level could result in significant lateral displacement.

## 3. Finite element analysis model

To evaluate the seismic-wave-caused lateral deformation in level liquefiable ground shown in Fig. 1(a) on a site scale, this section presents a plane-strain solid–fluid coupled finite element analysis model implemented in OpenSEES (McKenna and Fenves, 2001), an open-source software framework for earthquake engineering simulation. The 200 m × 50 m rectangular finite element saturated ground model is shown in Fig. 7(a), where each quadrilateral element with the u-p solid–fluid coupling formulation (Zienkiewicz and Shiomi, 1984) is 2 m × 1 m in size. The liquefiable soil composes a 160 m × 10 m rectangular region, at the ground surface in Fig. 7(a). The rest of the soil is non-liquefiable.

Liquefaction-caused lateral deformations are mostly observed in shallow layers near the ground surface, where the energy of Rayleigh wave is also concentrated, so the depth of liquefiable zone in Fig. 7 is set as 10 m. To reduce the constraint of non-liquefiable soil on the liquefiable soil to accommodate lateral deformation, and considering the attenuation of Rayleigh wave in liquefiable ground, the width of liquefiable zone is set as 160 m. As it is difficult to directly input realistic nonuniform seismic motion into plastic medium accurately, a non-liquefiable zone enclosing the liquefiable zone is used to allow for

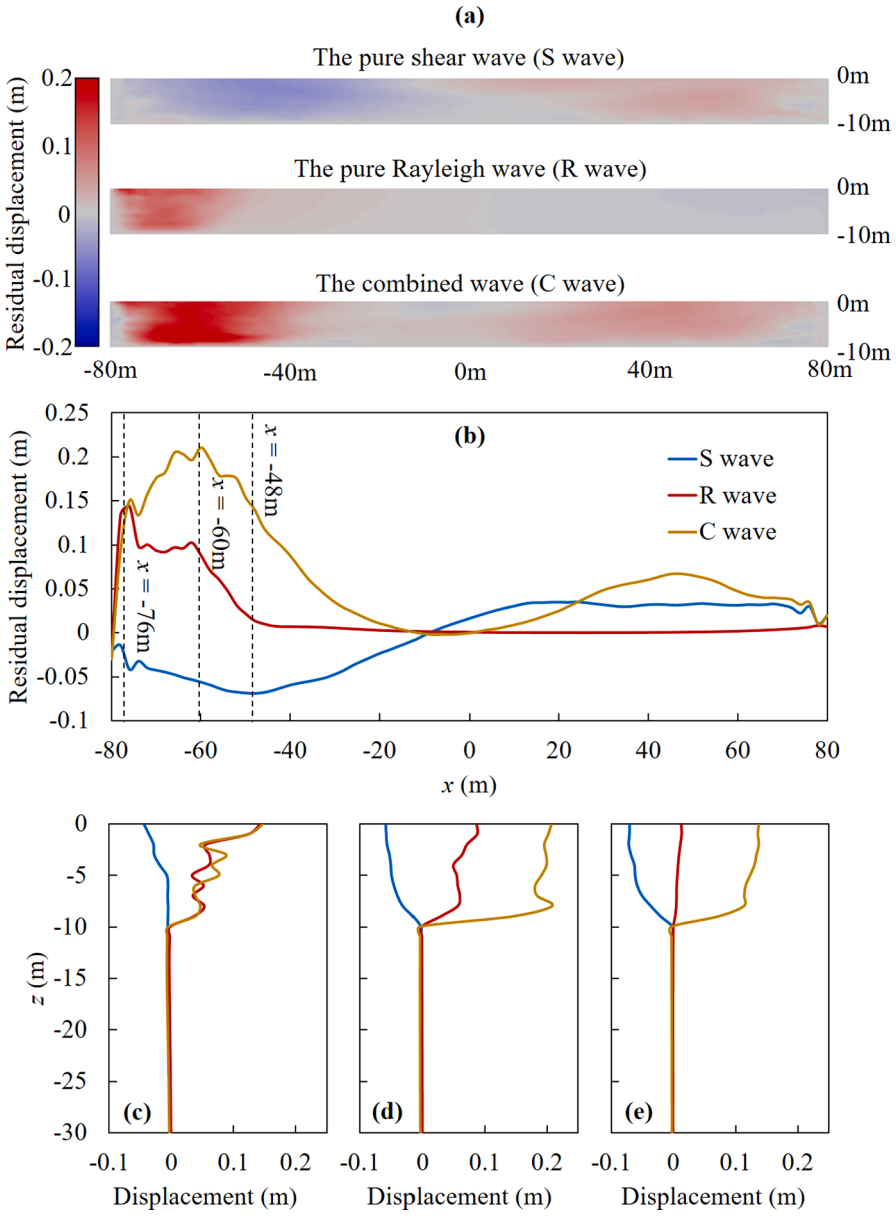


**Fig. 9.** Distributions of lateral residual displacement after shaking for the ground model under the pure shear wave, the pure Rayleigh wave, and the combination of shear wave and Rayleigh wave: (a) lateral residual displacement colourmap; (b) the lateral profile at the ground surface; (c) the vertical profile at $x$ = -76 m; (d) the vertical profile at $x$ = -60 m; (e) the vertical profile at $x$ = -48 m.

input of the seismic motions according to analytical solutions in elastic medium.

Free drainage condition is applied at the ground surface ($z$ = 0 m), while the other boundaries are undrained because the seepage discharge of the FEM model with low permeability coefficient is negligible (estimated to be less than $1 \times 10^{-5}$ m$^2$ in the 20 s computation period). Viscous-spring artificial boundary conditions (Liu et al., 2006), are introduced at the sides and base of the model to absorb scattered waves. Equivalent loads are applied on the left side for Rayleigh wave input (Fig. 7(b)), and at the base for shear wave input (Fig. 7(c)). This type of boundary condition has been shown to be effective for non-uniform seismic input into saturated domains under u-p formulation as the pore pressure wave velocity under this condition is close to zero (Li and Song, 2013). The determination of the parameters and equivalent loads of the artificial boundary condition is presented in more detail in Appendix B.

The permeability coefficients of the liquefiable and non-liquefiable zones are assumed to be $k = 1 \times 10^{-4}$ m/s and $k = 1 \times 10^{-8}$ m/s, respectively. The saturated density of both is $\rho = 2.0 \times 10^3$ kg/m$^3$. The non-liquefiable soil is modeled as an isotropic linear elastic material with Young's modulus $E$ = 50 MPa and Poisson's ratio $\upsilon$ = 0.4, corresponding to medium-stiff sandy clay. The liquefiable soil is modeled using the CycLiq model, with the parameters in Table 1. It should be noted that the choice of isotropic linear elastic model for the non-liquefiable soil is a simplification considering the focus of the study is on the behavior within the liquefiable zone. In the simulation results, the strain of the non-liquefiable soil is less than 0.6%, which makes the choice to omit nonlinearity acceptable (Mitchell, 1993).

For the numerical simulations using OpenSEES, the Krylov-Newton algorithm (Scott and Fenves, 2015) is employed to solve the nonlinear equations. The Hilber-Hughes-Taylor integration algorithm (Hilber et al., 1977) with $\alpha$ = 0.7 is used for time-domain integration. The penalty method with penalty factor $\alpha = 1 \times 10^{12}$ is introduced for constraints. Transient analysis is performed with variable time step.

As the actual seismogram recordings are usually a mixture of different types of seismic wave, it is difficult to decompose shear wave

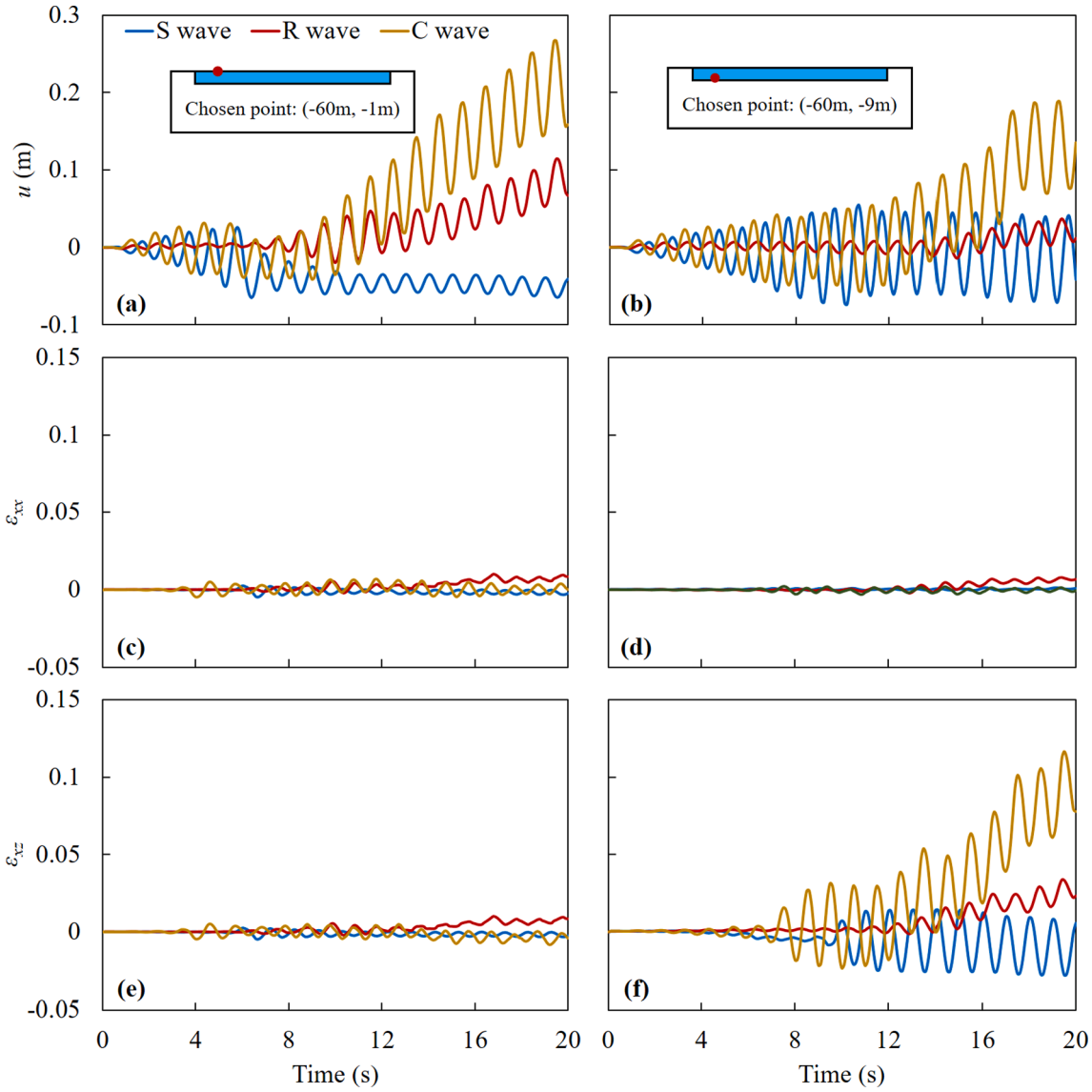


**Fig. 10.** Time histories of displacement and strain at typical locations under the three input waves: (a) lateral displacement $u_x$ at (-60 m, −1 m); (b) lateral displacement $u_x$ at (-60 m, −9 m); (c) horizontal normal strain $\varepsilon_{xx}$ at (-60 m, −1 m); (d) horizontal normal strain $\varepsilon_{xx}$ at (-60 m, −9 m); (e) shear strain $\varepsilon_{xz}$ at (-60 m, −1 m); (f) shear strain $\varepsilon_{xz}$ at (-60 m, −9 m).

and Rayleigh wave from these records, especially under complex geological conditions (Miller and Pursey, 1955). Therefore, sinusoidal motions are first used here to clearly distinguish the influence of the different wave types. The input motions as reference follow ramped sinusoidal time histories:

$$a_S = \begin{cases} t/10 \times A_{s0} sin(\omega_1 t + \theta) & t \leqslant 10s \\ A_{s0} sin(\omega_1 t + \theta) & 10s < t \leqslant 20s \end{cases} \tag{9a}$$

$$a_{Rx} = \begin{cases} t/10 \times A_{R0x} sin(\omega_2 t) & t \leqslant 10s \\ A_{R0x} sin(\omega_2 t) & 10s < t \leqslant 20s \end{cases} \tag{9b}$$

$$a_{Rz} = \begin{cases} t/10 \times A_{R0z} sin(\omega_2 t) & t \leqslant 10s \\ A_{R0z} sin(\omega_2 t) & 10s < t \leqslant 20s \end{cases} \tag{9c}$$

where $a_S$, $a_{Rx}$, and $a_{Rz}$ are the accelerations of the input shear wave, the horizontal component of Rayleigh wave, and the vertical component of Rayleigh wave, respectively. It is assumed that $\omega_1 = \omega_2 = 2\pi$ rad/s and $\theta = 0$, for a typical analysis. The input shear wave and Rayleigh wave acceleration time histories are shown in Fig. 8. The input shear wave (S wave) is uniform along the bottom boundary of the model following $a_S$ in Eq. (9-a), and the input Rayleigh wave (R wave) is non-uniform along the left boundary following $a_{Rx}$ and $a_{Rz}$ in Eq. (9-b) and Eq. (9-c). The average input acceleration amplitude along the ground depth under the Rayleigh wave is set to be equal to that of the input shear wave, i.e., $A_{R0} = \int_{-50}^{0} \sqrt{A_{R0x}^2(z) + A_{R0z}^2(z)} dz/50 = A_{S0}$, for a basis of comparison of the two types of input waves. For the combined wave (C wave) input, the input for the S wave and R wave are directly superimposed. This inevitably raises questions about whether the C wave case is comparable with the two other cases, which is later discussed in Section 5 by altering the input acceleration amplitudes.

## 4. Rayleigh wave-shear wave coupling induced level liquefiable ground lateral deformation

The displacement distributions in the liquefiable zone, the strains at typical locations, and the stresses at the location with maximum deformation in the finite element model under three types of input waves are presented in this section, to analyze the large lateral deformation phenomenon, mechanism, and influence of soil liquefaction, respectively.

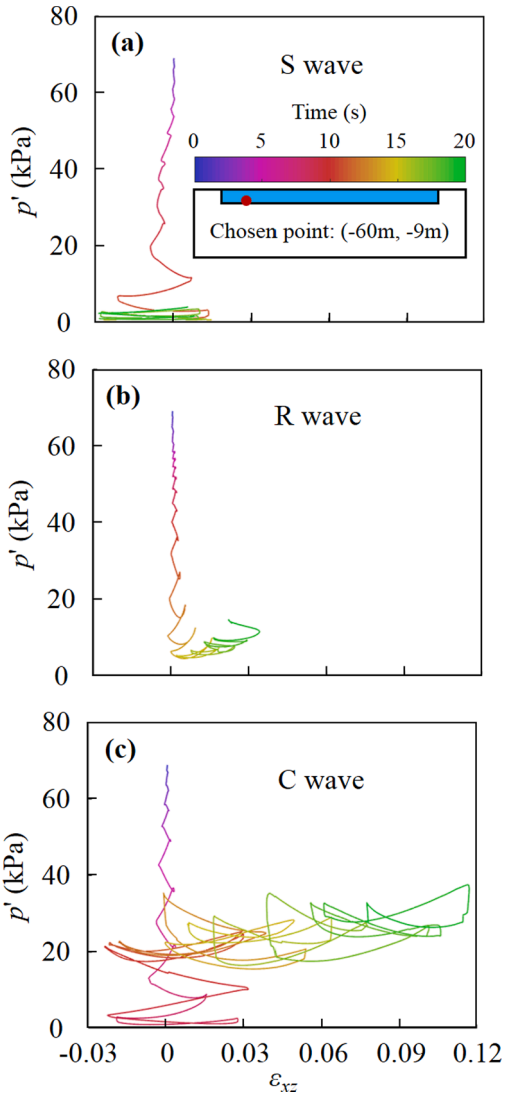


**Fig. 11.** Mean effective stresses $p'$ and shear strains $\varepsilon_{xz}$ under different waves for a chosen location (-60 m, −9 m). The colour of the line varies with time according to the legend.

### 4.1. Displacement distribution in the liquefiable zone

Distributions of lateral residual displacement after shaking for the ground model under the S wave, R wave, and C wave are shown in Fig. 9. The lateral residual displacement colourmaps within the liquefiable zone under the three different waves are plotted in Fig. 9(a).

A near symmetrical distribution of lateral residual displacement is observed within the liquefiable zone under the S wave (i.e., leftward in the left half of liquefiable zone and rightward in the right half) in Fig. 9 (a), whereas the distributions under the R wave and the C wave are asymmetrical. Under the R wave and the C wave, positive rightward residual displacement is observed (i.e., in the same direction as Rayleigh wave propagation).

The lateral residual displacement distributions at the ground surface under the three different inputs are plotted in Fig. 9(b). The maximum lateral residual displacement at the ground surface is 0.06 m at $x$ = -48 m under the S wave, 0.14 m at $x$ = -76 m under the R wave, and 0.21 m at $x$ = -60 m under the C wave, respectively. Positive lateral residual displacement occurs at the ground surface under the Rayleigh wave input, but decreases to less than 0.01 m at $x$ > -46 m. This indicates that the Rayleigh wave decays quickly in liquefiable soil, due to the decrease in the effective stress. If a shear wave is also involved, for the case of the combined wave, this lateral residual displacement is attained within a greater range, i.e., decreases to less than 0.01 m at $x$ > -20 m. Thus, Rayleigh wave-shear wave coupling not only amplifies the magnitude of lateral deformation within liquefiable soil, but also increases the area affected by the input motion.

Three vertical cross-sections, at $x$ = -76 m, $x$ = -60 m, and $x$ = -48 m, where the maximum residual displacement is observed under the three input waves are plotted in Fig. 9(c), Fig. 9(d), and Fig. 9(e), respectively. No residual displacement occurs within the linear elastic non-liquefiable soil (-30 m ≤ $z$ ≤ -10 m), as expected. Fig. 9(c) displays almost the same distributions of displacement along depth under the R wave and the C wave at $x$ = -76 m, highlighting the role of Rayleigh wave in displacement accumulation. However, the residual displacement caused by the C wave is more than three times that under the R wave at $x$ = -60 m and −48 m, with distinct depth distribution, as shown in Fig. 9(d) and (e). The displacement gradient, indicating shear strain, is significant near the interface between the liquefiable and non-liquefiable soils (i.e., $z$ = -10 m) under the combined wave.

### 4.2. Displacement, strain, and stress at typical locations

At $x$ = -60 m in Fig. 9(d), where the lateral deformation is largest under the C wave, two typical locations with different depths, $z$ = -9 m (i.e., near the interface between the liquefiable and non-liquefiable soils) and $z$ = -1 m (i.e., near the ground surface), are chosen to analyze the strains and displacements in detail. The time histories of lateral displacement, compression strain, and shear strain at these two locations under the three different input conditions are illustrated in Fig. 10, respectively.

Fig. 10 (a) and (b) plots the displacement time histories at the surface and base of the liquefiable zone under the three waves. The contribution of normal strain on lateral deformation is very small, visible from the normal strain time histories in Fig. 10 (c) and (d), agreeing with the element level analysis in Section 2. The accumulation of lateral deformation is mostly caused by the accumulation of shear strain near the interface between the liquefiable and non-liquefiable soils in Fig. 10 (f), whereas the shear strain at the surface is small (Fig. 10 (e)).

The contribution of soil liquefaction to the large lateral displacement is further investigated through the relationship between mean effective stress $p'$ and shear strain $\varepsilon_{xz}$ at the location (-60 m, −9 m) in Fig. 11, where the large lateral deformation appears under C wave. Under S wave (Fig. 11(a)), effective stress quickly decreases to below 20 kPa within 7 s, after which significant oscillatory shear strain is observed at liquefaction with negligible asymmetrical accumulation. Under R wave (Fig. 11(b)), effective stress below 20 kPa is reached much later, at 12 s, after which asymmetrical shear strain accumulation is observed. Under C wave (Fig. 11(c)), the shear wave component imposes quick effective stress decrease, reaching below 20 kPa within 5 s, while the combination of Rayleigh wave component with shear wave component induces significant asymmetrical shear strain accumulation.

Herein, an explanation for the large level ground lateral deformation observed in past earthquakes can be provided in full. Rayleigh wave can induce asymmetrical force within near surface soil, causing some asymmetrical lateral soil deformation. The coupling between Rayleigh wave and shear wave results in asymmetrical shear resistance within soil, to cause much greater lateral soil deformation. This lateral soil deformation induced by Rayleigh wave-shear wave coupling is significantly amplified in liquefiable soil, as soil degrades due to effective stress reduction.

Under the conditions here, the maximum strain in the site level model is less than 12%, yielding it adequate to use the small strain finite element method, as is adopted in this study. However, the influence of nonlinearity of the geometry may be non-negligible when greater strain is generated, where large strain formulations would be needed.

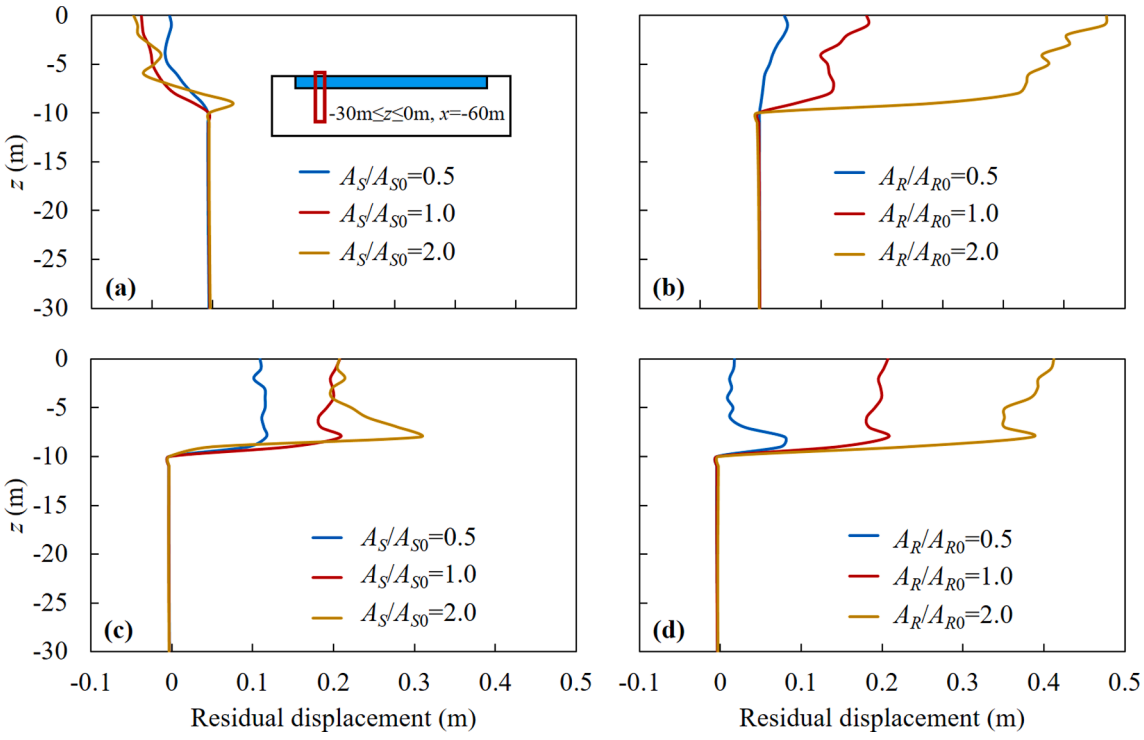


**Fig. 12.** Distribution of residual lateral displacement along depth at $x$ = -60 m and $-30\ \text{m} \le z \le 0$ m for different acceleration amplitude: (a) influence of $A_S$ under S wave; (b) influence of $A_R$ under R wave; (c) influence of $A_S$ under C wave; (d) influence of $A_R$ under C wave.

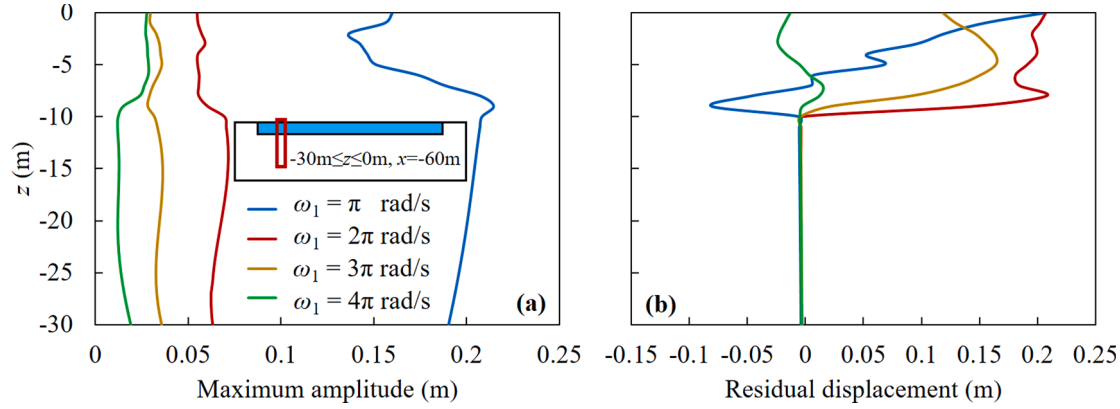


**Fig. 13.** Distribution of lateral displacement along depth at $x$ = -60 m and $-30\ \text{m} \le z \le 0$ m under different $\omega_1$: (a) distribution of maximum amplitude of dynamic lateral displacement; (b) distribution of residual lateral displacement.

## 5. Influence of input wave characteristics on lateral deformation

The analysis in Section 4 assumes that for the combined wave, the average input acceleration amplitude of the Rayleigh wave and that of the shear wave input are the same, while having the same frequencies as well, the phase difference between the two types of waves is not considered, i.e., $A_R = A_S$, $\omega_1 = \omega_2 = 2\pi$ rad/s, and $\theta = 0°$. Acceleration amplitude reflects the energy of the input wave, while frequency and phase difference of the two waves can also be of significant influence on soil deformation (Jibson and Tanyas, 2020), and are thus investigated in this section. At last, a simple composition of shear wave and Rayleigh wave based on actual seismograms in both vertical and horizontal directions is executed and input into the finite element model for comparison with the sinusoidal input.

### 5.1. Acceleration amplitude $A_S$ and $A_R$

The analysis for the S, R, and C waves in Section 4 are based on the assumption that $A_S$ and $A_R$ are equal. Under this assumption, one may argue that the increase in residual lateral displacement for the C wave case is due to its stronger input motion rather than the effect of Rayleigh wave-shear wave coupling. To address this, the influence of input acceleration amplitudes is assessed. For S wave input, $A_S$ is changed with respect to $A_{S0}$. For R wave, $A_R$ is changed with respect to $A_{R0}$. For C wave, both $A_S$ and $A_R$ are changed.

The residual lateral displacement for different input acceleration amplitudes at $x$ = -60 m and $-30\ \text{m} \le z \le 0$ m under the S, R, and C waves are shown in Fig. 12 (a), Fig. 12 (b), and Fig. 12 (c) and (d), respectively. The results clearly show that changing the input S wave acceleration amplitude has very limited influence on the residual displacement in the liquefiable ground when $A_S/A_{S0}$ is between 0.5 and 2. In contrast, for R wave, increase in input $A_R$ significantly affects

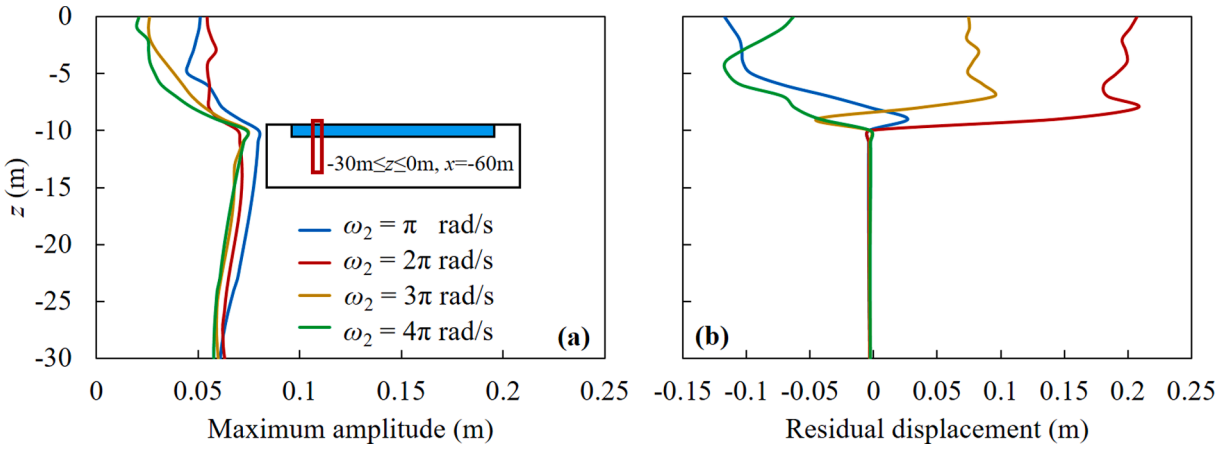


**Fig. 14.** Distribution of lateral displacement along depth at $x$ = -60 m and $-30$ m $\leq z \leq 0$ m under different $\omega_2$: (a) distribution of maximum amplitude of dynamic lateral displacement; (b) distribution of residual lateral displacement.

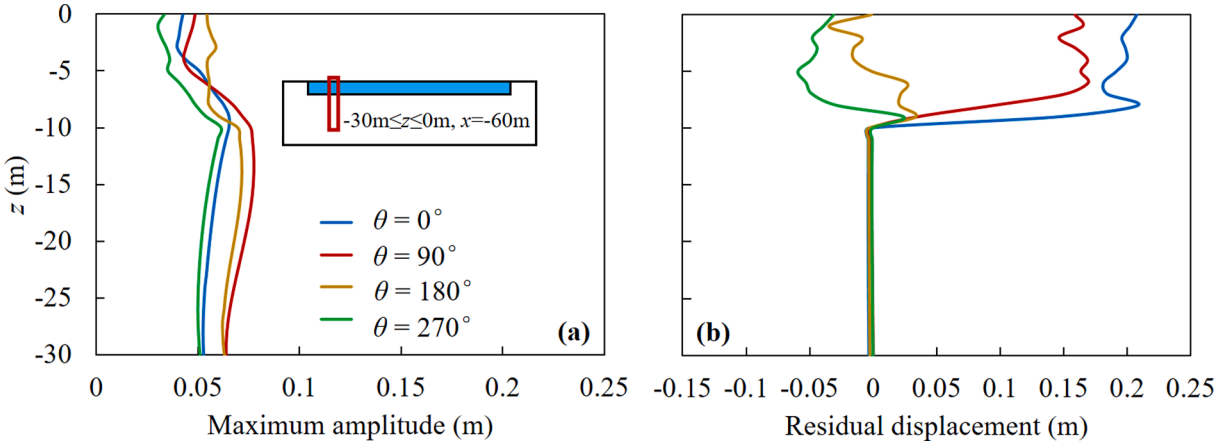


**Fig. 15.** Distribution of lateral displacement along depth at $x$ = -60 m and $-30$ m $\leq z \leq 0$ m under different $\theta$: (a) distribution of maximum amplitude of dynamic lateral displacement; (b) distribution of residual lateral displacement.

residual displacement. When $A_R/A_{R0}$ = 2.0, the surface residual displacement becomes three times that for $A_{R0}$. For C wave, the residual displacement is again relatively insensitive to shear wave amplitude change, while being very sensitive to Rayleigh wave amplitude change. These results clearly highlight that the increased residual displacement observed for the R and C waves compared with that of the S wave are not simply due to input acceleration amplitude differences, and justifies the Rayleigh wave-shear wave coupling mechanism as a cause for the large level ground lateral deformation.

### 5.2. Frequency $\omega_1$ and $\omega_2$

The influence of frequency of the Rayleigh wave and the shear wave and phase difference between them is also investigated in subsection 5.2 and 5.3. The same displacement distributions as those in Fig. 12, but for different $\omega_1$, $\omega_2$, and $\theta$, are shown in Fig. 13, Fig. 14, and Fig. 15, respectively. Fig. 13 (a) shows that the dynamic lateral displacement under $\omega_1 = \pi$ rad/s, i.e., frequency $f_1$ = 0.5 Hz, is significantly greater than other conditions. This is because the input shear wave frequency is close to the fundamental frequency of the ground, which is 0.55 Hz.

Fig. 13 (b) displays different levels of residual lateral deformation under different $\omega_1$. When $\omega_1 = \pi$ rad/s, the residual lateral displacement in liquefiable soil is negative near the interface between liquefiable soil and non-liquefiable soil, and positive near the ground surface. The negative displacement near the interface is likely due to the relatively strong response induced by the shear wave under this condition, and corresponds to the negative residual displacement for pure shear wave input in Fig. 9. As depth decreases, the effect of the Rayleigh wave becomes more prominent and generates positive residual displacement.

When $\omega_1 = 4\pi$ rad/s, i.e., $\omega_1 = 2\omega_2$, the residual lateral displacement is much smaller than the other cases (Fig. 13 (b)). The cause for this phenomenon is that although the Rayleigh wave is still asymmetrical, every half cycle of the Rayleigh wave is overlapped by a complete cycle of the symmetrical shear wave, resulting in a mostly symmetrical soil response. These analyses indicate that the frequency of the shear wave significantly affects dynamic displacement, while the relative relationship between the frequencies of the shear wave and the Rayleigh wave affects the accumulation of residual displacement.

The results in Fig. 14 shows that the frequency of the Rayleigh wave has relatively small influence on dynamic displacement (Fig. 14 (a)), while significantly affecting residual displacement (Fig. 14 (b)). For $\omega_2 = 2\pi$ rad/s and $3\pi$ rad/s, positive residual displacement accumulation is observed as is in Section 4. For $\omega_2 = \pi$ rad/s or $4\pi$ rad/s, the residual lateral displacement is negative, similar to that under pure shear wave in Fig. 9. This indicates that greater lateral residual displacement is generated when the frequencies of the Rayleigh wave and the shear wave are closer.

### 5.3. Phase difference $\theta$

From Fig. 15, for $\theta = 0°$ or 90°, the accumulation of residual displacement is significant. However, the residual displacement is much

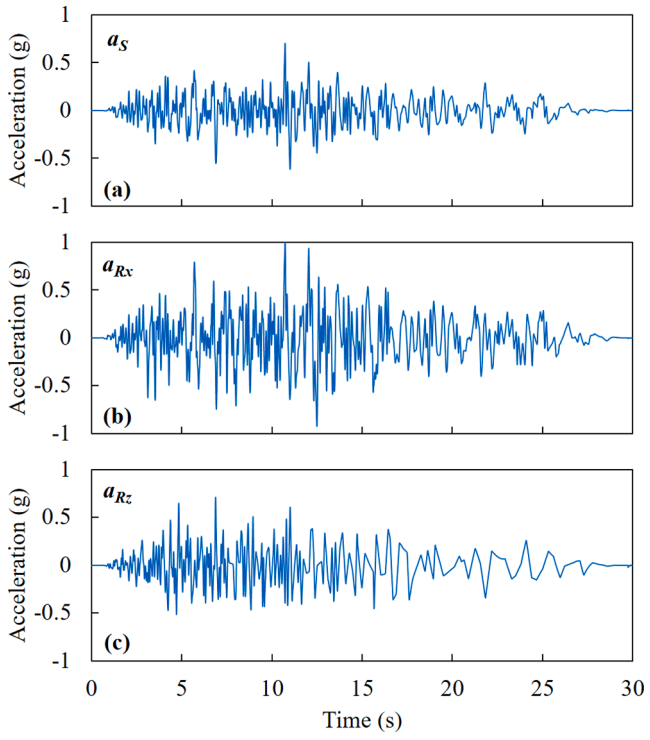


**Fig. 16.** Input shear wave and Rayleigh wave acceleration time histories based on the 1971 San Fernando Earthquake: (a) input shear wave at the bottom boundary of the model; (b) horizontal component of input Rayleigh wave on the surface; (b) vertical component of input Rayleigh wave on the surface.

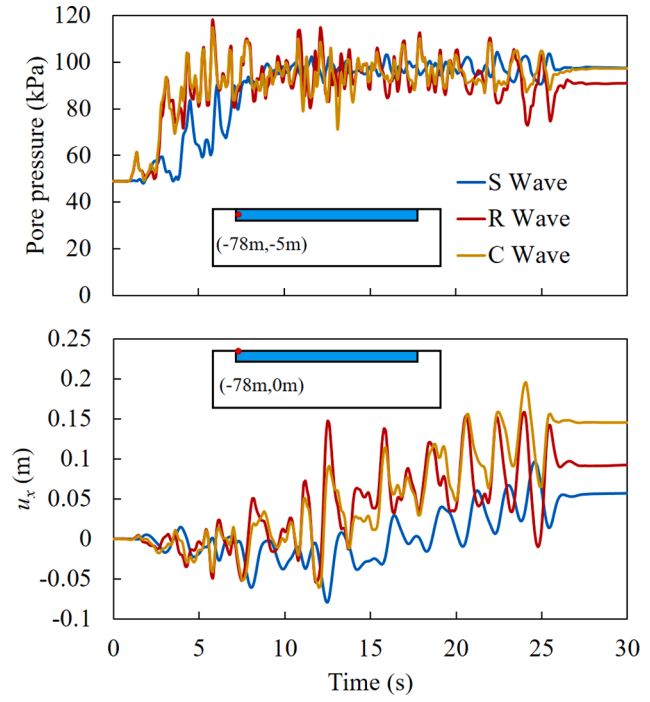


**Fig. 17.** Time histories of pore pressure and lateral displacement under S Wave, R Wave, and C Wave based on actual seismograms: (a) pore pressure at the point (-78 m, −5 m); (b) lateral displacement of the points (-78 m, 0 m).

smaller for $\theta = 180°$ or 270°, which is caused by the asymmetrical Rayleigh wave becoming symmetrical with respect to the shear wave. As the phase difference between the two types of waves is affected by the ground characteristics and the distance from the seismic source, this

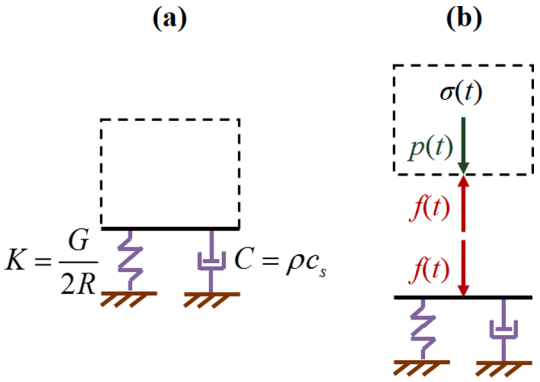


**Fig. B1.** The schematic diagram for non-uniform seismic input: (a) the viscous-spring artificial boundary condition; (b) computational method for equivalent loads.

indicates that the accumulation of lateral displacement in the ground is site specific and location dependent.

### 5.4. Input wave based on realistic earthquake recordings

The previous analysis is based on sinusoidal wave input, which is convenient for the analysis of the basic mechanism but different from realistic earthquake ground motions. The seismic recordings during the 1971 San Fernando Earthquake, where Rayleigh wave was clearly observed (Canitez and Toksoz, 1972), are applied to the model in Fig. 7 and used here as a more realistic example. The seismograms data from the Pasadena-CIT Athenaeum Station (Ancheta, et al. 2013) are used (Fig. 16). The input shear wave and Rayleigh wave acceleration time histories are back calculated from the vertical and horizontal acceleration time histories based on the method of energy partition proposed by Miller and Pursey (1955), which is presented in more detail in Appendix C.

Fig. 17 (a) plots the time histories of computed pore pressure at the point (-78 m, −5 m) under S wave, R wave, and C wave based on actual seismograms. The chosen point is near to the source of Raleigh wave because the Rayleigh wave decays quickly for this recorded ground motion. The pore pressure exceeds 100 kPa at 5 s under C wave and R wave, and at 9 s under S wave, indicating liquefaction at 5 m depth. Note the earlier liquefaction initiation under R wave and C wave is likely due to the greater acceleration amplitude of the Rayleigh wave back calculated from the recorded ground motion. The lateral displacement at point (-78 m, 0 m) is shown in Fig. 17 (b). The lateral displacement under C Wave exhibits significantly greater accumulation towards the positive rightward direction compared with S and R waves, and the residual lateral displacements after shaking are 0.05 m, 0.09 m, and 0.15 m under S wave, R wave, and C wave, respectively. These results obtained using realistic earthquake recordings further confirms the findings from the sinusoidal input, highlighting the Rayleigh wave-shear wave coupling mechanism for large lateral deformation in level liquefiable ground.

## 6. Conclusions

Motivated by the observations of large lateral deformation in almost level liquefiable ground during past strong earthquakes, this study proposed the coupling of Rayleigh wave and shear wave as a mechanism for this phenomenon. Rayleigh wave-shear wave coupling is proved to play an important role in the accumulation of large lateral deformation in level liquefiable ground on a simple element level and a site level.

The simple element level elasto-plastic force–displacement model revealed conceptually that Rayleigh waves can induce asymmetrical compression force within near surface soils, and cause an asymmetrical

shear resistance within soil when coupled with shear waves. The asymmetric compression force induced by Rayleigh waves alone can cause asymmetrical lateral deformation, but is limited in value. The combination of the symmetrical shear force induced by shear wave with the asymmetrical shear resistance is the major contributor for the accumulation of lateral deformation. The element level analysis using the CycLiq constitutive model further confirmed this mechanism valid for liquefiable soil.

The finite element analysis used the CycLiq constitutive model for liquefaction behavior of sand and viscous-spring artificial boundary conditions. The site level numerical results agreed with the findings in the element level model. The numerical results further indicated the importance of soil liquefaction on lateral displacement, where the degradation of liquefiable soil amplifies the lateral displacement accumulation caused by Rayleigh wave and shear wave coupling. Large shear strain is shown to be mainly concentrated near the interface between liquefiable and non-liquefiable soil.

The frequencies of the shear wave and the Rayleigh wave and their phase difference were shown to be influential to the accumulation of lateral displacement. The residual lateral displacement is greater when the frequencies of the two types of waves are closer and the phase difference between the two types of waves are at $\theta = 0^{\circ}$ and $90^{\circ}$.

It must be pointed out that Rayleigh wave-shear wave coupling induced lateral deformation is one source of the large lateral deformation in almost level liquefiable ground observed during strong earthquakes. Many other factors may contribute to this phenomenon, e.g., geological conditions, irrigation, etc. The numerical analysis in this study adopted small strain finite element method, where the accumulation of lateral deformation is limited by the analysis method. Further studies should conduct using numerical methods supporting large deformation (Chen and Tong, 2014; Jie et al., 2008) to more realistically simulate the observations from recent earthquake events.

*CRediT authorship contribution statement*

**Yunyi Li:** Data curation, Investigation, Writing – original draft. **Chao Luo:** Conceptualization, Writing – review & editing. **Jian-Min Zhang:** Supervision, Writing – review & editing. **Fang Liu:** Writing – review & editing. **Rui Wang:** Conceptualization, Writing – original draft, Writing – review & editing.

## Declaration of Competing Interest

The authors declare that they have no known competing financial interests or personal relationships that could have appeared to influence the work reported in this paper.

## Acknowledgments

The authors would like to thank the National Natural Science Foundation of China (No. 52022046 and No. 52038005) and the State Key Laboratory of Hydroscience and Hydraulic Engineering (No. 2021-KY-04) for funding this study. The second author acknowledges the support from the Natural Science Foundation of Hebei Province (No. E2019210350), the State Key Laboratory of Mechanical Behavior and System Safety of Traffic Engineering Structures (No. ZZ2020-04 and ZZ2021-03).

## Appendix A. . Analytical solution for the linear elastic element level model

For a single degree of freedom forced vibration model under harmonic load using linear elastic constitutive relation and linear damping, the equation of motion is:

$$m\ddot{u} + c\dot{u} + ku = p_0 sin\omega t \tag{A1}$$

where $m$ is the mass, $c$ is the damping coefficient, $k$ is the stiffness coefficient, $u$ is the displacement, $p_0$ and $\omega$ are the amplitude and circular frequency of the load, respectively. The general solution of equation (A1) can be expressed as:

$$u(t) = exp(-\varsigma\omega_n t)(Acos\omega_D t + Bsin\omega_D t) + Ccos\omega t + Dsin\omega t \tag{A2}$$

where $\varsigma = c/(2m\omega_n)$ is the damping ratio, $\omega_n = \sqrt{k/m}$, $\omega_D = \omega_n\sqrt{1-\varsigma^2}$. The value of parameters A and B are determined by the initial state of motion, C and D are determined from the particular solution for the steady state.

For the element level model under S wave in subsection 2.3, $m = 2 \times 10^3$ kg, $c = 8 \times 10^4$N/(m/s), $k = 2 \times 10^7$N/m, $p_0 = 2 \times 10^4$N, $\omega = 2\pi$ rad/s. Considering the initial state of motion is $u(0) = 0$ and $\dot{u}(0) = 0$, the analytical solution under S wave is:

$$u = \left[1.00 \times 10^{-3} sin(6.28t) - 6.31 \times 10^{-5} sin(97.98t) exp(-20.00t)\right]\mathrm{m} \tag{A3}$$

Similarly, the analytical solution under R wave for $n\mathrm{s} \leqslant t \leqslant (n+1/2)\mathrm{s}$ is:

$$\left[5.00 \times 10^{-5} sin(6.28t) - 7.03 \times 10^{-7} sin(446.76t) exp(-20.12(t-n))\right]\mathrm{m} \tag{A4}$$

While for $(n+1/2)\mathrm{s} \leqslant t \leqslant (n+1)\mathrm{s}$, the solution is:

$$\left[\left(-4.57 \times 10^{-5} sin(6.87(t-n-1/2))\right) exp(-20.00(t-n-1/2))\right]\mathrm{m} \tag{A5}$$

where $n = 0,1,2,\ldots,9$.

## Appendix B. . Rayleigh wave input method

The method for determining the parameters of the artificial boundary conditions and the equivalent loads is presented here in brief. The general displacement solution of a 2-D cylindrical shear wave in the polar coordinate system can be expressed as:

$$u(r,t) = f(r - c_s t)/\sqrt{r} \tag{B1}$$

where $c_s$ is the shear wave velocity of the media and $r$ is the distance to the source.

The velocity solution is:

$$\dot{u}(r,t) = -c_s f'(r-c_s t)/\sqrt{r} \tag{B2}$$

The shear stress in this wave field follows:

$$\tau(r,t) = G\partial u/\partial r = G[-f(r-c_s t)/2r\sqrt{r} + f'(r-c_s t)/\sqrt{r}] \tag{B3}$$

Substituting Eq. (B.1) and Eq. (B.2) into Eq. (B.3), the shear stress at $r = R$ can be expressed as:

$$\tau(R,t) = -(G/2R)u(R,t) - \rho c_s \dot{u}(R,t) \tag{B4}$$

From Eq. (B.4), it can be found that the shear wave propagating perpendicularly to the artificial boundary will be completely absorbed if the artificial boundary is set as a spring with stiffness coefficient $K = G/2R$ and a damper with damping coefficient $C = \rho c_s$, as shown in Fig. B1(a). A similar artificial boundary condition can also be determined for compression waves.

Fig. B.1(b) depicts the method for computing the equivalent load $p(t)$ applied at the boundary element. To generate the displacement $u(t)$ under a given seismic excitation, the equivalent load $p(t)$ applied on the boundary element should be in balance with the resistance $f(t)$ caused by the viscous-spring artificial boundary condition and the stress $\sigma(t)$ at the boundary element caused by the seismic input:

$$p(t) = \sigma(t) + f(t) \tag{B5}$$

where $f(t)$ can be determined by substituting $u(t)$ into Eq. (B.4), and $\sigma(t)$ can be determined by substituting $u(t)$ into the geometric and the constitutive equations.

Taking Rayleigh wave as an example, the analytical solutions of displacements under Rayleigh wave can be expressed as:

$$u_x = \xi A[exp(-\alpha z) - 2\alpha\beta/(\beta^2+\xi^2)exp(-\beta z)]sin(\omega t - \xi x) \tag{B.6a}$$

$$u_z = -\alpha A[exp(-\alpha z) - 2\xi^2/(\beta^2+\xi^2)exp(-\beta z)]cos(\omega t - \xi x) \tag{B.6b}$$

$$\alpha = \sqrt{\xi^2 - \xi_1^2}, \beta = \sqrt{\xi^2 - \xi_2^2} \tag{B.6c}$$

where $\xi$, $\xi_1$, and $\xi_2$ are the wavenumbers of Rayleigh wave, P wave, and S wave, respectively. $A$ is a parameter for displacement amplitude. From the solutions of displacements, the stresses can be calculated through constitutive relation and geometric equations:

$$\sigma_{xx} = A\{[\lambda\alpha^2 - (\lambda+2G)\xi^2]exp(-\alpha z) + G(\beta^2+\xi^2)exp(-\beta z)\}cos(\omega t - \xi x) \tag{B.7a}$$

$$\tau_{xz} = -2G\alpha\xi A[exp(-\alpha z) - exp(-\beta z)]sin(\omega t - \xi x) \tag{B.7b}$$

Therefore, the equivalent forces for Rayleigh wave can be expresses as:

$$p_x(t,z) = \sigma_{xx}(t,z)\,|_{x=0} + (\lambda+2G)/2Ru_x(t,z)\,|_{x=0} + \rho c_p \dot{u}_x(t,z)\,\Big|_{x=0} \tag{B.8a}$$

$$p_z(t,z) = \tau_{xz}(t,z)\,|_{x=0} + G/2Ru_z(t,z)\,|_{x=0} + \rho c_s \dot{u}_z(t,z)\,\Big|_{x=0} \tag{B.8b}$$

The artificial boundary conditions and the equivalent loads are developed for single phase solid materials. For a saturated poroelastic media, Biot (1956) confirmed that two forms of compression wave exist, one propagates in solid phase and the other propagates in fluid phase. Li and Song (2013) found that the compression wave propagating in fluid phase decays quickly if the permeability coefficient of the saturated poroelastic media is less than $10^{-3}$m/s, and the frequency of the input wave is less than 10 Hz. Both of these conditions are satisfied in this study. Thus, the method presented here can be used for the saturated ground in this study.

Strictly speaking, the influence of the free field around the model should also be considered in the artificial boundary condition. However, analysis shows that the influence of the equivalent loads caused by the free field is very limited and is omitted in this study.

## Appendix C. . Wave decomposition method for actual seismic recording

A simplified method for decomposing shear wave and Rayleigh wave based on actual seismograms is presented here in brief. The actual velocity seismograms are generally composed of two orthogonal horizontal components $\vec{v}_\alpha$ and $\vec{v}_\beta$, and a vertical component $\vec{v}_z$. For the 2-D model in this study, the velocity of S wave on the ground surface is mainly in the horizontal direction, and is marked as $\vec{v}_{Sx}$. Correspondingly, the horizontal and vertical velocity components of R wave are marked as $\vec{v}_{Rx}$ and $\vec{v}_{Rz}$, respectively. Coupling of P wave is neglected here for its greater wave velocity. The wave decomposition must first satisfy:

$$\begin{cases} \vec{v}_{Rx} + \vec{v}_{Sx} = \vec{v}_\alpha + \vec{v}_\beta \\ \vec{v}_{Rz} = \vec{v}_z \end{cases} \tag{C1}$$

Another condition is used in the decomposition based on the partition of energy between elastic waves proposed by Miller and Pursey (1955). For a single-element source, the quantities of power radiated in S wave $W_S$ and R wave $W_R$ are presented as:

$$\begin{cases} W_S = K\int_0^{\pi/2} \Theta_S(\theta)\Theta_S^*(\theta)sin\theta d\theta \\ W_R = K\int_{-\infty}^{0} X(-\omega/c_R z)d(-\omega/c_R z) \end{cases} \tag{C2}$$

The constant $K$ and functions $\Theta_S(\theta)$, $\Theta_S^*(\theta)$, and $X(-\omega/c_R z)$ are related to the elastic modulus and Poisson's ratio of the elastic ground, the details of which are rather complex and could referred to in Miller and Pursey (1955). Thus, the ratio of R wave energy to S wave energy is given by:

$$\left(\overrightarrow{v}_{Rx}^2 + \overrightarrow{v}_{Rz}^2\right) \Big/ \overrightarrow{v}_{Sx}^2 = W_R/W_s \tag{C3}$$

Theoretically, $\overrightarrow{v}_{Sx}$, $\overrightarrow{v}_{Rx}$,and $\overrightarrow{v}_{Rz}$ could be solved through formula (C.1) and (C.3). The equations for wave decomposition is then presented as:

$$\begin{cases} v_{Rz} = v_z \\ v_{Rx} = (2\left(\overrightarrow{v}_\alpha + \overrightarrow{v}_\beta\right)\cdot\overrightarrow{m} + v_{Rz})/3 \\ v_{Sx} = \left(\overrightarrow{v}_\alpha + \overrightarrow{v}_\beta\right)\cdot\overrightarrow{m} - v_{Rx} \end{cases} \tag{C4}$$

where the unit vector $\overrightarrow{m}$ is parallel to the direction of maximum velocity.

## References


Ancheta, T.D., Darragh, R.B., Stewart, J.P., Seyhan, E., Silva, W.J., Chiou, B.-J., Wooddell, K.E., Graves, R.W., Kottke, A.R., Boore, D.M., Kishida, T., Donahue, J.L., 2014. NGA-West2 Database. Earthquake Spectra 30 (3), 989–1005.

Arulanandan, K., Scott, R.F., 1993. Project velacs—control test results. J. Geotech. Eng. 119 (8), 1276–1292. https://doi.org/10.1061/(ASCE)0733-9410(1993)119:8(1276).

Biot, M.A., 1956. Theory of propagation of elastic waves in a fluid saturated porous solid: I Low-frequency range. J. Acoust. Soc. Am. 28 (2), 168–178. https://doi.org/10.1121/1.1908239.

Bradley, K., Mallick, R., Andikagumi, H., Hubbard, J., Meilianda, E., Switzer, A., Du, N., Brocard, G., Alfian, D., Benazir, B., Feng, G., Yun, S.-H., Majewski, J., Wei, S., Hill, E. M., 2019. Earthquake-triggered 2018 Palu Valley landslides enabled by wet rice cultivation. Nat. Geosci. 12 (11), 935–939. https://doi.org/10.1038/s41561-019-0444-1.

Brune, J.N., Pomeroy, P.W., 1963. Surface wave radiation patterns for underground nuclear explosions and small-magnitude earthquakes. J. Geophys. Res. 68 (17), 5005–5028. https://doi.org/10.1029/JZ068i017p05005.

Canitez, N., Toksoz, M.N., 1972. Static and dynamic study of earthquake source mechanism: San Rernando earthquake. J. Geophys. Res. 77 (14), 2583–2594. https://doi.org/10.1029/JB077i014p02583.

Chen, W., Tong, Q., 2014. Simulation of earthquake-induced slope deformation using SPH method. Int. J. Numer. Anal. Meth. Geomech. 38 (3), 297–330. https://doi.org/10.1002/nag.2218.

Chiaro, G., Kiyota, T., Koseki, J., 2013. Strain localization characteristics of loose saturated Toyoura sand in undrained cyclic torsional shear tests with initial static shear. Soils Found. 53 (1), 23–34. https://doi.org/10.1016/j.sandf.2012.07.016.

Cui, J., Men, F. L., and Wang, X., 2004. Soil Liquefaction induced by Rayleigh Waves. 13th World Conference on Earthquake Engineering Vancouver, B.C., Canada.

Eberhard, M. O., Baldridge, S., Marshal, J., Mooney, W., and Rix, G. J., 2010. The MW 7.0 Haiti earthquake of January 12, 2010. USGS/EERI Advance Reconnaissance Team Report 2010-1048.

Fang, H. Q., Wang,. Z. Q., and Zao. S. D., 1979. Macroscopic mechanism of soil liquefaction and its influence on earthquake damage of ground, Proc. 26th Int. Geol. Cong.

Gallant, A.P., Montgomery, J., Mason, H.B., Hutabarat, D., Reed, A.N., Wartman, J., Irsyam, M., Simatupang, P.T., Alatas, I.M., Prakoso, W.A., Djarwadi, D., Hanifa, R., Rahardjo, P., Faizal, L., Harnanto, D.S., Kawanda, A., Himawan, A., Yasin, W., 2020. The Sibalaya Flowslide initiated by the 28 September 2018 M W 7.5 Palu-Donggala, Indonesia Earthquake. Landslides 17 (8), 1925–1934. https://doi.org/10.1007/s10346-020-01354-1.

Hamada, M., 1992. Large ground deformations and their effects on lifelines: 1964 Niigata earthquake case studies of liquefaction and lifelines performance during past earthquake. Technical Report NCEER-92-0001, National Centre for Earthquake Engineering Research, Buffalo.

Han, B., Ampuero, J.-P., Meng, L., Fielding, E.J., Liang, C., Milliner, C.W.D., Feng, T., Huang, H., 2019. Early and persistent supershear rupture of the 2018 magnitude 7.5 Palu earthquake. Nat. Geosci. 12 (3), 200–205. https://doi.org/10.1038/s41561-018-0297-z.

He, B., Zhang, J.M., Li, W., Wang, R., 2020. Numerical analysis of LEAP centrifuge tests on sloping liquefiable ground: influence of dilatancy and post-liquefaction shear deformation. Soil Dyn. Earthquake Eng. 137 (2020), 106288 https://doi.org/10.1016/j.soildyn.2020.106288.

Hilber, H.M., Hughes, T.J.R., Taylor, R.L., 1977. Improved numerical dissipation for time integration algorithms in structural dynamics. Earthquake Eng. Struct. Dyn. 5 (3), 283–292.

Iai, S., 2018. Evaluation of performance of port structures during earthquakes. Soil Dyn. Earthquake Eng. 126, 105192. https://doi.org/10.1016/j.soildyn.2018.04.055.

Jiang, M., Kamura, A., Kazama, M., 2021. Comparison of liquefaction behavior of granular material under SH-and Love-wave strain conditions by 3D DEM. Soils Found. 61 (5), 1235–1250. https://doi.org/10.1016/j.sandf.2021.06.013.

Jibson, R.W., Tanyaş, H., 2020. The influence of frequency and duration of seismic ground motion on the size of triggered landslides—A regional view. Eng. Geol. 273, 105671. https://doi.org/10.1016/j.enggeo.2020.105671.

Jie, Y., Tang, X., Luan, M., Yang, Q., 2008. Adaptive element free Galerkin method applied to analysis of earthquake induced liquefaction. Earthquake Engineering and Engineering Vibration 7 (2), 217–224. https://doi.org/10.1007/s11803-008-0790-2.

Kiyota, T., Furuichi, H., Hidayat, R. F., Tada, N., and Nawir, H. 2020. Overview of long-distance flow-slide caused by the 2018 sulawesi earthquake, indonesia. Soils and Foundations, 60(3). https://doi.org/ 10.1016/j.sandf.2020.03.015.

Kusumawardani, R., Chang, M., Upomo, T.C., Huang, R.-C., Fansuri, M.H., Prayitno, G. A., 2021. Understanding of Petobo liquefaction flowslide by 2018.09.28 Palu-Donggala Indonesia earthquake based on site reconnaissance. Landslides 18 (9), 3163–3182.

Kutter, B. L., Manzari, M. T., and Zeghal, M., 2020. Model Tests and Numerical Simulations of Liquefaction and Lateral Spreading. LEAP-UCD-2017.

Li, P., Song, E.X., 2013. A high-order time-domain transmitting boundary for cylindrical wave propagation problems in unbounded saturated poroelastic media. Soil Dyn. Earthquake Eng. 48, 48–62. https://doi.org/10.1016/j.soildyn.2013.01.006.

Liu, H., Zhang, J.-M., Zhang, X., Wang, R., 2020. Seismic performance of block-type quay walls with liquefiable calcareous sand backfill. Soil Dyn. Earthquake Eng. 132, 106092. https://doi.org/10.1016/j.soildyn.2020.106092.

Liu, J.B., Du, Y.X., Du, X.L., Wang, Z.Y., Wu, J., 2006. 3D viscous-spring artificial boundary in time domain. Earthquake Engineering and Engineering Vibration 5 (1), 93–102. https://doi.org/10.1007/s11803-006-0585-2.

Lombardo, L., Tanyas, H., 2020. Chrono-validation of near-real-time landslide susceptibility models via plug-in statistical simulations. Eng. Geol. 278, 105818. https://doi.org/10.1016/j.enggeo.2020.105818.

Men, F.L., 1992. Wave propagation in saturated soil layer and sand liquefaction. Collected Research papers in Earthquake Engineering. Seismology Press, Beijing.

McKenna, F., Fenves, G.L., 2001. OpenSees manual. PEER Center. <http://OpenSees.berkeley.edu>.

Miller, G.F., Pursey, G., 1955. On the partition of energy between elastic waves in a semi-infinite solid. Proc. Royal Soc. London 233 (1192), 55–69. https://doi.org/10.2307/99853.

Mitchell, J.K., 1993. Fundamentals of soil behavior-2nd Edition. John Wiley & Sons Inc.

Pei, X., Zhang, X., Guo, B., Wang, G., Zhang, F., 2017. Experimental case study of seismically induced loess liquefaction and landslide. Eng. Geol. 223, 23–30. https://doi.org/10.1016/j.enggeo.2017.03.016.

Sassa, S., Takagawa, T., 2019. Liquefied gravity flow-induced tsunami: first evidence and comparison from the 2018 Indonesia Sulawesi earthquake and tsunami disasters. Landslides 16 (1), 195–200. https://doi.org/10.1007/s10346-018-1114-x.

Scott, M.H., Fenves, G.L., 2015. Krylov subspace accelerated Newton algorithm: application to dynamic progressive collapse simulation of frames. J. Struct. Eng. 136 (5), 473–480. https://doi.org/10.1061/(ASCE)ST.1943-541X.0000143.

Socquet, A., Hollingsworth, J., Pathier, E., Bouchon, M., 2019. Evidence of supershear during the 2018 magnitude 7.5 Palu earthquake from space geodesy. Nat. Geosci. 12 (3), 192–199. https://doi.org/10.1038/s41561-018-0296-0.

Staroszczyk, R., 1996. Pore pressure generation and liquefaction in saturated sands due to the propagation of surface waves. Acta Geophysica Polonica 44 (2), X7–218.

Staroszczyk, R., 2016. Rayleigh waves transformation in liquefying water-saturated sands. Arch. Hydro-Eng. Environm. Mechanics 63 (2–3), 173–190. https://doi.org/10.1515/heem-2016-0011.

Wang, R., Fu, P., Zhang, J.M., 2016. Finite element model for piles in liquefiable ground. Comput. Geotech. 72, 1–14. https://doi.org/10.1016/j.compgeo.2015.10.009.

Wang, R., Zhang, J.M., Wang, G., 2014. A unified plasticity model for large post-liquefaction shear deformation of sand. Comput. Geotech. 59 (2014), 54–66. https://doi.org/10.1016/j.compgeo.2014.02.008.

Wang, R., Cao, W., Xue, L., Zhang, J.-M., 2021. An anisotropic plasticity model incorporating fabric evolution for monotonic and cyclic behavior of sand. Acta Geotech. 16 (1), 43–65. https://doi.org/10.1007/s11440-020-00984-y.

Wang, Y.Z., Feng, W.P., Chen, K., Samsonov, S., 2019. Source characteristics of the 28 September 2018 Mw 7.4 Palu, Indonesia, Earthquake derived from the Advanced Land Observation Satellite 2 Data. Remote Sensing 11 (17), 1999. https://doi.org/10.3390/rs11171999.

Wang, Z.Q., Fang, H.Q., Zhao, S.D., 1983. Macroscopic features of earthquake induced soil liquefaction and its influence on ground damage. Can. Geotech. J. 20 (1), 61–68. https://doi.org/10.1139/t83-007.

Watkinson, I.M., Hall, R., 2019. Impact of communal irrigation on the 2018 palu earthquake-triggered landslides. Nat. Geosci. 12 (11), 940–945. https://doi.org/10.1038/s41561-019-0448-x.

Wolf, J.P., 1985. Dynamic Soil-Structure Interaction, Printice-. Hall Inc.

Yolsal-Cevikbilen, S., Taymaz, T., 2019. Source characteristics of the 28 September 2018 M w 7.5 Palu-Sulawesi, Indonesia (SE Asia) Earthquake based on inversion of teleseismic bodywaves. Pure Appl. Geophys. 176 (10), 4111–4126. https://doi.org/10.1007/s00024-019-02294-1.

Yoshida, N., Watanabe, H., Yasuda, S., Mora-Castro, S., 1992. Liquefaction-induced ground failure and related damage to structures during 1991 Telire-Limon. Costa Rica Earthquake. Technical Report Nceer 1 (92–0019), 37–52.

Zhang, J.M., Tokimatsu, K., 1998. Methods for evaluating residual post-liquefaction ground settlement and horizontal displacement. Soils Foundations 38 (Special), 69–83.

Zhang, J.M., Wang, G., 2012. Large post-liquefaction deformation of sand, Part I: physical mechanism, constitutive description and numerical algorithm. Acta Geotech. 7 (2), 67–113. https://doi.org/10.1007/s11440-011-0150-7.

Zhu, T., Wang, R., Zhang, J.M., 2021. Evaluation of various seismic response analysis methods for underground structures in liquefiable sand. Tunn. Undergr. Space Technol. 110 (2021), 103803.

Zienkiewicz, O.C., Shiomi, T., 1984. Dynamic behaviour of saturated porous media; the generalized biot formulation and its numerical solution. Int. J. Numer. Anal. Meth. Geomech. 8 (1), 71–96. https://doi.org/10.1002/nag.1610080106.